A Conservative Fourth-Order Real Space Method for the (2+1)D Dirac Equation

Emile Vanderstraeten[a,*], Dries Vande Ginste[a]

[a] *quest, IDLAB, Department of Information Technology, Ghent University/imec, Technologiepark-Zwijnaarde 126, Ghent, Belgium*

Abstract

Modelling the time-dependent (2+1)D Dirac equation has recently gained importance since this equation effectively describes multiple condensed matter systems. To avoid the large dispersion errors of second-order real space schemes, a highly accurate method is presented here instead. The method utilises a fourth-order central difference on a staggered grid and an explicit symplectic Partitioned Runge-Kutta (PRK) time integrator. In contrast to traditional Runge-Kutta (RK) time stepping, no unphysical dissipation is introduced into the simulation. Moreover, it is demonstrated, both theoretically via Poisson maps and numerically, that the novel scheme has excellent conservation properties. Furthermore, the proposed numerical method is provably stable and the dispersion error is low and isotropic. Several interesting numerical examples are presented. Besides validating the advocated method, they also showcase its computational efficiency and low memory consumption.

Keywords:
Dirac equation, Higher-order FDTD, Partitioned Runge-Kutta, Conservative methods, Poisson integrator, Numerical dispersion and stability

1. Introduction

Since its first description by Paul Dirac in 1928 [1], the Dirac equation has been one of the fundamental equations in modern physics. It describes the motion of a quantum spin-$1/2$ particle in a Lorentz invariant manner, unifying the fields of special relativity and quantum mechanics. In contrast to the Schrödinger equation, it incorporates the concept of spin in a natural way and it is able to explain the fine structure corrections in the spectrum of hydrogenic atoms. The negative-energy solutions to the equation imply the existence of antimatter, a special form of matter that was unknown at the time but experimentally verified by the observation of the positron four years later [2]. Besides the existence of antiparticles, other peculiar phenomena can be attributed to the Dirac equation such as the Zitterbewegung [3] and Klein tunneling [4].

Even though the Dirac equation was originally derived for relativistic, quantum mechanical systems, it has recently sparked the interest of several other research domains, as Dirac-like equations emerge there as well [5]. A well-known example is graphene. Based on a tight-binding approach to describe the bandstructure of the honeycomb lattice, together with the assumption of low-energy excitations near the band extrema, charge carriers in graphene are modelled by a massless Dirac equation in which the speed of light is replaced by the Fermi velocity [6]. Similar behaviour was identified in other 2D materials, such as silicene, germanene, borophene and transition metal dichalcogenides [7, 8, 9]. As the Dirac-like behaviour of the charge carriers is related to the trigonal symmetry of the lattice, another set of Dirac equations is retrieved when this symmetry is superimposed on a system in an artificial way [5]. For instance, electrons in an external, periodic hexagonal potential [10] and cold atoms in a honeycomb optical lattice [11] are described by a Dirac equation. Besides two-dimensional (2D) materials, also topological insulators are attracting a lot of attention lately because of the appearance of Dirac surface states at their boundaries with normal insulators or vacuum [12]. Given that the time-dependent Dirac equation occurs more and more in various physical systems and that analytical

*Corresponding author
Email address: Emile.Vanderstraeten@UGent.be (Emile Vanderstraeten)

solutions are scarce, one identifies the need for accurate and efficient numerical schemes. Since the aforementioned physical systems are all 2D, this paper focuses on the (2+1)D Dirac equation.

Several numerical schemes have been proposed to solve the time-dependent Dirac equation. These schemes can be classified on whether they are real space or momentum space methods, or a combination of both. A full momentum space approach is given in [13]. Nonetheless, most approaches involving the momentum space combine it with the real space via the split-operator formalism [14, 15, 16, 17, 18, 19, 20, 21]. These numerical schemes approximate the time evolution operator by a sequence of operators that depend on either the momentum or the spatial variables, as both types of operators have an analytical expression in their respective spaces. Nevertheless, such a scheme requires changing back and forth between real and momentum space via the Fast Fourier Transform (FFT). Various real space techniques have been developed as well, for instance the finite element method of [22], several finite difference schemes [23, 24, 25] and a scheme based on the method of characteristics [26]. However, real space approaches are typically plagued by the appearance of spurious solutions, which is called the fermion doubling problem [22, 26, 27]. It relates to the presence of multiple Dirac cones in the numerical energy-momentum dispersion relation instead of a single one as in the continuous case. To reduce the fermion doubling problem, finite difference schemes that employ a staggered grid [28, 29, 30, 31, 32] have been constructed. Even though these approaches do not fully avoid the fermion doubling problem, they are still advantageous computationally because of the reduced number of unknowns [33]. The main drawback of the above-mentioned, staggered schemes is that they are only second-order accurate in space and time, resulting in large dispersion errors.

To resolve the issue of large dispersion errors, a higher-order technique may be adopted. These are especially suitable for wave propagation problems where errors accumulate in time [34]. A first, natural attempt to construct a higher-order real space numerical scheme for the (2+1)D Dirac equation could be to employ the spatial grid of [29], together with a higher-order stencil to approximate the spatial derivative and to march in time with an explicit Runge-Kutta (RK) integrator. Nevertheless, we show in this paper that such a scheme has troublesome conservation properties and is thus not applicable to long-term simulations. Instead, we propose to utilise a geometric integrator. A numerical method is called geometric if it preserves one or more geometric or physical properties of the underlying system exactly, within machine precision. For instance, the numerical scheme could preserve the total energy, total momentum, total probability, time reversal symmetry, phase-space volume, symplectic structure, Poisson structure, etc [35, 36]. In literature, several geometric integrators have been presented which focus on preservation of energy [35, 37, 38] or symplectic structure [36, 39, 40]. These last ones were originally developed for Hamiltonian problems in classical mechanics but are now widespread in simulations in several domains of research, being molecular dynamics [41], cosmology [42], electromagnetics [43, 44], non-relativistic quantum mechanics [45, 46] and multiphysics [47].

In this paper, we propose a new higher-order method utilising an explicit, symplectic Partitioned Runge-Kutta (PRK) method for the time-dependent (2+1)D Dirac equation. The method is provably stable and exhibits a low and isotropic phase error. First, the staggered grid of [29] is employed to discretise the spatial variables. Next, the set of ordinary differential equations (ODEs), obtained after this spatial discretisation, is rewritten in a particular form to facilitate an explicit, symplectic PRK approach. Even though the time evolution operator of this specific set of ODEs is not a symplectic but a Poisson map, employing symplectic PRK methods is still advantageous as we show that these numerical methods retain the Poisson property of the time evolution operator. Moreover, we demonstrate that momentum is conserved exactly as well, while probability and energy are nearly conserved. Also, in addition to the excellent long-term properties, we illustrate that the new method is computationally efficient, both in terms of memory consumption and total computation time, by comparing it to a RK based higher-order method and the leapfrog method of [29].

This paper is organised as follows. In Section 2 we introduce the spatial discretisation. Section 3 proceeds with a discussion of the problems related to time stepping based on the RK method, while Section 4 presents the new method. Its stability and dispersion are investigated in Section 5 and Section 6. This is followed by a study, both analytically and numerically, of the conservation laws in Section 7. In Section 8, the novel numerical scheme is validated and compared to other schemes by means of several, interesting simulation examples. Finally, Section 9 concludes the paper.

2. Spatial discretisation of the (2+1)D Dirac equation

Given that many physical systems under interest are 2D, we restrict ourselves to the (2+1)D Dirac equation for a spin-1/2 particle, given by

$$\begin{aligned} \imath\hbar\frac{\partial}{\partial t}\mathbf{\Psi}(x,y,t) &= \hat{\mathbf{H}}(x,y)\,\mathbf{\Psi}(x,y,t) \\ &= \left(c\boldsymbol{\sigma}_x\hat{p}_x + c\boldsymbol{\sigma}_y\hat{p}_y + \boldsymbol{\sigma}_z mc^2 + \mathbf{I}_2 V(x,y)\right)\mathbf{\Psi}(x,y,t)\,, \end{aligned} \tag{1}$$

where $\hat{\mathbf{H}}$ is the Hamiltonian operator and $\hat{p}_x = -\imath\hbar\frac{\partial}{\partial x}$ and $\hat{p}_y = -\imath\hbar\frac{\partial}{\partial y}$ the momentum operators. The wave function $\mathbf{\Psi}$ consists of two components in the (2+1)D Dirac equation, which are denoted by u and v. The matrices $\boldsymbol{\sigma}_x$, $\boldsymbol{\sigma}_y$ and $\boldsymbol{\sigma}_z$ are the Hermitian, anti-commuting Pauli matrices, given by $\left(\begin{smallmatrix}0&1\\1&0\end{smallmatrix}\right)$, $\left(\begin{smallmatrix}0&-\imath\\\imath&0\end{smallmatrix}\right)$ and $\left(\begin{smallmatrix}1&0\\0&-1\end{smallmatrix}\right)$ respectively, while $\mathbf{I}_2$ is the 2×2 identity matrix. Furthermore, the mass and potential are given by m and V. The presence of the reduced Planck constant $\hbar$ and the speed of light c indicates that ideas of both quantum mechanics and special relativity are incorporated into the Dirac equation. The SI unit system is used in all mathematical expressions and in the description of the novel formalism. In all simulations we employ atomic units (a.u.), i.e., $\hbar = m_e = 1$ and $c = 137.036$, instead. The probability density of the wave function is defined by $\mathbf{\Psi}^\dagger(x,y)\,\mathbf{\Psi}(x,y) = |u(x,y)|^2 + |v(x,y)|^2$. The integral of the probability density over the entire simulation domain, i.e., the total probability, is equal to one and stays constant over time as we are considering a single particle in a closed quantum mechanical system. Besides conservation of the total probability, energy is conserved as well under the condition that the Hamiltonian $\hat{\mathbf{H}}$ is time independent. However, total momentum is only conserved when we additionally require the mass and potential to be explicitly position independent because momentum and position operators do not commute.

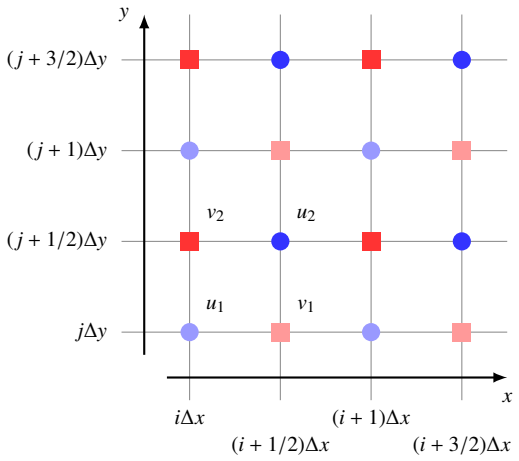

Figure 1: Illustration of the staggered spatial grid of [29]. For each unit cell (i, j), the component u is defined at two positions: $(x = i\Delta x, y = j\Delta y)$ and $(x = (i + 1/2)\,\Delta x, y = (j + 1/2)\,\Delta y)$. The first one is denoted by u_1; the second one by u_2. Similarly, for component v, we get v_1 at position $(x = (i + 1/2)\,\Delta x, y = j\Delta y)$ and v_2 at $(x = i\Delta x, y = (j + 1/2)\,\Delta y)$.

We utilise the staggered spatial grid of [29], which is depicted in Fig. 1. All values related to u_1 are collected in a column vector $\mathbf{u}_1$ with dimension N_xN_y, where N_x and N_y are the number of cells in the x- and y-direction, respectively. Similarly, column vectors $\mathbf{u}_2$, $\mathbf{v}_1$ and $\mathbf{v}_2$ are constructed. In contrast to [29], we apply a *fourth-order* central difference approximation to the spatial derivatives in (1) and terminate the system by periodic boundaries to obtain the following system of equations

$$\frac{\mathrm{d}\mathbf{y}}{\mathrm{d}t} = \mathbf{L}\,\mathbf{y}, \tag{2}$$

with

$$\mathbf{L} = \frac{1}{\imath\hbar}\begin{pmatrix} mc^2\mathbf{I}_{N_xN_y} + \mathbf{V}_{\mathbf{u}_1} & 0 & -\imath\hbar c\mathbf{D}_{4,x} & -\hbar c\mathbf{D}_{4,y} \\ 0 & mc^2\mathbf{I}_{N_xN_y} + \mathbf{V}_{\mathbf{u}_2} & \hbar c\mathbf{D}_{4,y}^T & \imath\hbar c\mathbf{D}_{4,x}^T \\ \imath\hbar c\mathbf{D}_{4,x}^T & \hbar c\mathbf{D}_{4,y} & -mc^2\mathbf{I}_{N_xN_y} + \mathbf{V}_{\mathbf{v}_1} & 0 \\ -\hbar c\mathbf{D}_{4,y}^T & -\imath\hbar c\mathbf{D}_{4,x} & 0 & -mc^2\mathbf{I}_{N_xN_y} + \mathbf{V}_{\mathbf{v}_2} \end{pmatrix} \quad \text{and} \quad \mathbf{y} = \begin{pmatrix} \mathbf{u}_1 \\ \mathbf{u}_2 \\ \mathbf{v}_1 \\ \mathbf{v}_2 \end{pmatrix}. \tag{3}$$

The matrix $\mathbf{D}_{4,x}$ is the numerical analogue of the spatial derivative along x and is given by the Kronecker product $\mathbf{d}_{4,x} \otimes \mathbf{I}_{N_y}$, where the order is determined by the structure of the vectors $\mathbf{u}_1$, $\mathbf{u}_2$, $\mathbf{v}_1$ and $\mathbf{v}_2$. The expression for $[\mathbf{d}_{4,x}]_{i,j}$ is given by

$$\frac{1}{24\Delta x}\left(\delta_{i,j-2} - 27\delta_{i,j-1} + 27\delta_{i,j} - \delta_{i,j+1}\right), \tag{4}$$

with δ the Kronecker delta symbol. The matrix $\mathbf{D}_{4,y}$ is defined in a similar way: $\mathbf{I}_{N_x} \otimes \mathbf{d}_{4,y}$. The values of the potential V at the positions of $\mathbf{u}_1$ are contained in the diagonal matrix $\mathbf{V}_{\mathbf{u}_1}$. In a similar way, we obtain $\mathbf{V}_{\mathbf{u}_2}$, $\mathbf{V}_{\mathbf{v}_1}$ and $\mathbf{V}_{\mathbf{v}_2}$. We now apply a time stepping method to (2).

3. Runge-Kutta (RK) time stepping

A first, straightforward higher-order numerical method to solve (2) is the RK4 time integrator [34]. The main novelty of this paper does, however, not reside in the construction of an RK based method. Still, we implemented an RK4 scheme as a reference method and the details of this scheme, including its stability and dispersion analysis, are provided in Appendix A. In this section, it is explained why RK schemes are not well suited to tackle the (2+1)D Dirac equation. The reason is twofold. Firstly, RK methods divide one large time step into smaller substeps or stages. All substep values are stored as they are required to complete one large time step. The storage of each intermediate step makes the RK method computationally expensive in terms of memory consumption, as illustrated in Section 8. Secondly, an even more detrimental issue with the RK method as time stepping method for (2) occurs when performing long-term simulations. To illustrate the problematic behaviour, we consider a simple simulation of a free particle wherein we track the total probability. The initial wave function is a gaussian wave packet of the form

$$\mathbf{\Psi}(t=0,x,y) = N\begin{pmatrix}1\\C\end{pmatrix}\exp\left(\frac{\imath p_{x,0}x}{\hbar}\right)\exp\left(-\frac{(x-x_0)^2}{4\sigma_x^2}\right)\exp\left(\frac{\imath p_{y,0}y}{\hbar}\right)\exp\left(-\frac{(y-y_0)^2}{4\sigma_y^2}\right), \tag{5}$$

with N a normalisation constant and C given by

$$\frac{c\left(p_{x,0} + \imath p_{y,0}\right)}{mc^2 + \sqrt{m^2c^4 + \left(p_{x,0}^2 + p_{y,0}^2\right)c^2}}. \tag{6}$$

The total probability is obtained by integrating the probability density over the spatial domain. As we are dealing with discrete variables in the numerical RK scheme, the integration is approximated by a summation according to

$$\int_{-\infty}^{+\infty}\int_{-\infty}^{+\infty} |u|^2 + |v|^2 \mathrm{d}x\,\mathrm{d}y \approx \frac{\Delta x\,\Delta y}{2}\left(\mathbf{u}_1^\dagger\mathbf{u}_1 + \mathbf{u}_2^\dagger\mathbf{u}_2 + \mathbf{v}_1^\dagger\mathbf{v}_1 + \mathbf{v}_2^\dagger\mathbf{v}_2\right) = \mathcal{P}. \tag{7}$$

To analyse the evolution of this total probability $\mathcal{P}$, we calculate at every time step n the relative error, defined by $E_{\mathcal{P}}(n) = \frac{|\mathcal{P}(n)-\mathcal{P}(0)|}{|\mathcal{P}(0)|}$. In Fig. 2a we demonstrate the issue with RK time stepping for (2). The total probability vanishes over time, leading to an increasing error $E_{\mathcal{P}}(n)$, which severely restricts the number of time steps in a reliable simulation. Increasing the number of time steps further would eventually lead to the complete disappearance of the particle. The error on the total momentum and total energy, which is not shown here, behaves in a similar way.

This unfavourable behaviour is related to the numerical dispersion and the corresponding numerical frequency ω_{num}, given by (A.9), which contains an *imaginary component*. Indeed, via (A.5), one obtains that $R(\pm\imath|D|\Delta t)$ is not located on the unit circle. Therefore, ω_{num} of (A.9) is a complex number and its imaginary part $\mathrm{Im}(\omega_{\text{num}})$ introduces dissipation into the simulation. The magnitude of this numerical artifact can be reduced by decreasing the time step. As the

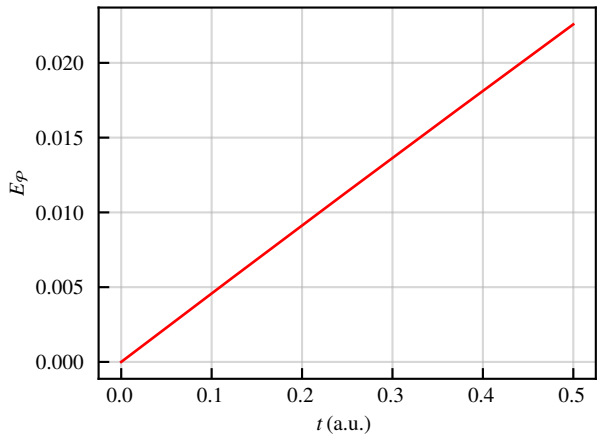

(a) Evolution of the relative error on the total probability $\mathcal{P}$ over time. As parameters for the initial wave function (5), expressed in a.u., $m = 0$, $x_0 = y_0 = 0$, $p_{x,0} = 4, p_{y,0} = 0$ and $\sigma_x = \sigma_y = 1$ were taken. The simulation domain ranges from -10 to 10 in the x- and y-direction, while N_x and N_y are equal to 200, leading to a spatial step $\Delta x = \Delta y = 0.1$. The corresponding time step, determined by the stability condition (A.8), is $\Delta t = 6.257\,10^{-4}$. After 800 time steps, the error already exceeds 2%.

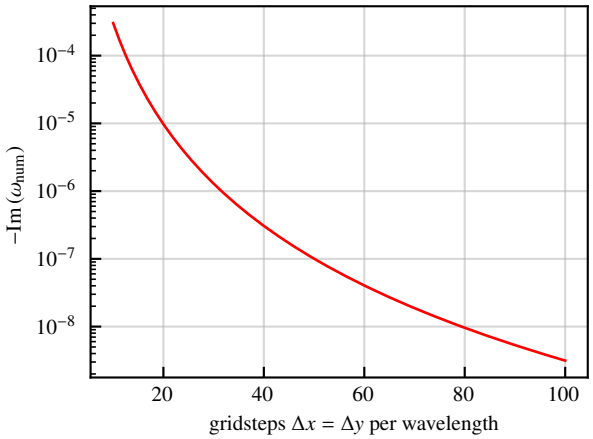

(b) Imaginary part of (A.9) as a function of the number of gridsteps per de Broglie wavelength. The employed time step is related to the spatial step via the stability condition (A.8).

Figure 2: Illustration of the dissipative nature of the numerical scheme employing RK time stepping.

spatial and time step are intimately related through the stability condition (A.8), employing a smaller spatial step has a similar effect (see Fig. 2b). Still, this approach enlarges the total computation time of the simulation considerably. Therefore, in this paper, we construct a new method based on geometric integrators, effectively avoiding violations of the conservation laws.

4. Partitioned Runge-Kutta (PRK) time stepping

To mitigate the aforementioned issues, we now present a novel scheme based on explicit, symplectic PRK time stepping. First, in general, we introduce this PRK time stepping approach for the following system of ODEs:

$$\begin{aligned} \frac{\mathrm{d}\mathbf{q}}{\mathrm{d}t} &= \mathbf{g}\left(\mathbf{p}\right) \\ \frac{\mathrm{d}\mathbf{p}}{\mathrm{d}t} &= \mathbf{f}\left(\mathbf{q}\right). \end{aligned} \tag{8}$$

If a Hamiltonian $H(\mathbf{q}, \mathbf{p})$ can be found such that $\mathbf{g} = \nabla_{\mathbf{p}} H\left(\mathbf{q}, \mathbf{p}\right)$ and $\mathbf{f} = -\nabla_{\mathbf{q}} H\left(\mathbf{q}, \mathbf{p}\right)$, the set of equations (8) reduces to a Hamiltonian system. These special systems, originating from classical mechanics, have the property that the time evolution operator is a symplectic map [48]. A linear map $\mathbf{\Phi} : \mathbb{R}^{2d} \mapsto \mathbb{R}^{2d} : \left(\begin{smallmatrix}\mathbf{q}\\ \mathbf{p}\end{smallmatrix}\right) \mapsto \mathbf{A}\left(\begin{smallmatrix}\mathbf{q}\\ \mathbf{p}\end{smallmatrix}\right)$, with $\mathbf{A} \in \mathbb{R}^{2d\times 2d}$ and d the dimension of $\mathbf{p}$ and $\mathbf{q}$, is called symplectic if $\mathbf{A}$ satisfies

$$\mathbf{A}^T \mathbf{J}\, \mathbf{A} = \mathbf{J}, \quad \text{with} \quad \mathbf{J} = \begin{pmatrix} 0 & \mathbf{I}_d \\ -\mathbf{I}_d & 0 \end{pmatrix}. \tag{9}$$

Requiring a RK method to conserve this property inevitably leads to an implicit scheme, while PRK methods can be symplectic and explicit [40]. Even though these explicit, symplectic PRK methods were originally developed for Hamiltonian systems [40], we consider them an alluring option for general systems of the form (8) as well, because of the low memory consumption and good long-term properties. Application of such a PRK method to (8) leads to

the following time stepping scheme:

$$\begin{array}{cc} \mathbf{Q}^{n,0} = \mathbf{q}^n & \mathbf{P}^{n,1} = \mathbf{p}^n \\ \mathbf{Q}^{n,1} = \mathbf{Q}^{n,0} + \Delta t\, B_1\, \mathbf{g}\left(\mathbf{P}^{n,1}\right) & \mathbf{P}^{n,2} = \mathbf{P}^{n,1} + \Delta t\, b_1\, \mathbf{f}\left(\mathbf{Q}^{n,1}\right) \\ \mathbf{Q}^{n,2} = \mathbf{Q}^{n,1} + \Delta t\, B_2\, \mathbf{g}\left(\mathbf{P}^{n,2}\right) & \mathbf{P}^{n,3} = \mathbf{P}^{n,2} + \Delta t\, b_2\, \mathbf{f}\left(\mathbf{Q}^{n,2}\right) \\ \vdots & \vdots \\ \mathbf{Q}^{n,s} = \mathbf{Q}^{n,s-1} + \Delta t\, B_s\, \mathbf{g}\left(\mathbf{P}^{n,s}\right) & \mathbf{P}^{n,s+1} = \mathbf{P}^{n,s} + \Delta t\, b_s\, \mathbf{f}\left(\mathbf{Q}^{n,s}\right) \\ \mathbf{q}^{n+1} = \mathbf{Q}^{n,s} & \mathbf{p}^{n+1} = \mathbf{P}^{n,s+1} \end{array} \tag{10}$$

[40, 49], where the intermediate values are denoted by capital letters. An explicit, symplectic PRK method is thus characterised by the coefficients b_i and B_i, where i ranges from 1 to s, the number of stages or substeps. These methods alternate between updating the variables related to $\mathbf{p}$ and those related to $\mathbf{q}$. In contrast to RK time stepping, intermediate values are not stored, because in every substep the previous intermediate values are replaced by the new ones. Consequently, memory usage is reduced significantly.

Now, we construct a novel scheme based on an explicit, symplectic PRK integrator for the (2+1)D time-dependent Dirac equation. Thereto, we reformulate (2) by splitting $\mathbf{u}_1$, $\mathbf{u}_2$, $\mathbf{v}_1$ and $\mathbf{v}_2$ into their real and imaginary parts and by introducing a particular choice for $\mathbf{q}$ and $\mathbf{p}$:

$$\mathbf{q} = \begin{pmatrix} \mathrm{Im}\left(\mathbf{u}_1\right) \\ \mathrm{Re}\left(\mathbf{u}_2\right) \\ \mathrm{Re}\left(\mathbf{v}_1\right) \\ \mathrm{Im}\left(\mathbf{v}_2\right) \end{pmatrix} \text{ and } \mathbf{p} = \begin{pmatrix} \mathrm{Re}\left(\mathbf{u}_1\right) \\ \mathrm{Im}\left(\mathbf{u}_2\right) \\ \mathrm{Im}\left(\mathbf{v}_1\right) \\ \mathrm{Re}\left(\mathbf{v}_2\right) \end{pmatrix}, \tag{11}$$

which leads to

$$\begin{aligned} \frac{\mathrm{d}\mathbf{q}}{\mathrm{d}t} &= \mathbf{K}\,\mathbf{p} \\ \frac{\mathrm{d}\mathbf{p}}{\mathrm{d}t} &= -\,\mathbf{K}^T\mathbf{q}, \end{aligned} \tag{12}$$

with

$$\mathbf{K} = \frac{1}{\hbar}\begin{pmatrix} -mc^2\mathbf{I}_{N_xN_y} - \mathbf{V}_{\mathbf{u}_1} & 0 & -\hbar c\mathbf{D}_{4,x} & \hbar c\mathbf{D}_{4,y} \\ 0 & mc^2\mathbf{I}_{N_xN_y} + \mathbf{V}_{\mathbf{u}_2} & \hbar c\mathbf{D}_{4,y}^T & \hbar c\mathbf{D}_{4,x}^T \\ \hbar c\mathbf{D}_{4,x}^T & \hbar c\mathbf{D}_{4,y} & -mc^2\mathbf{I}_{N_xN_y} + \mathbf{V}_{\mathbf{v}_1} & 0 \\ \hbar c\mathbf{D}_{4,y}^T & -\hbar c\mathbf{D}_{4,x} & 0 & mc^2\mathbf{I}_{N_xN_y} - \mathbf{V}_{\mathbf{v}_2} \end{pmatrix}. \tag{13}$$

Hence, we succeeded at recasting (2) into the form (8), enabling the usage of explicit, symplectic PRK methods. A single time step for the particular system (12) corresponds to

$$\begin{pmatrix} \mathbf{q}^{n+1} \\ \mathbf{p}^{n+1} \end{pmatrix} = \mathbf{T}\begin{pmatrix} \mathbf{q}^n \\ \mathbf{p}^n \end{pmatrix} = \left(\prod_{N=1}^{s}\begin{pmatrix} 1 & 0 \\ -\Delta t b_N \mathbf{K}^T & 1 \end{pmatrix}\begin{pmatrix} 1 & \Delta t B_N \mathbf{K} \\ 0 & 1 \end{pmatrix}\right)\begin{pmatrix} \mathbf{q}^n \\ \mathbf{p}^n \end{pmatrix}, \tag{14}$$

where $\mathbf{T}$ is the amplification matrix of the scheme[1].

We opt here for an efficient PRK method [50] of which the coefficients b_i and B_i are given in Table 1[2]. It exploits the First Same As Last (FSAL) principle, i.e., the last substep of a certain entire step can be concatenated with the first substep of the next entire step because $b_5 = 0$, reducing the number of effective stages of the method to four. Given

[1] To resolve the ambiguity related to the product operator because of the non-commutativity of the matrix multiplication, the convention that the sequence is built up from right to left, is adopted.

[2] Due to the particular structure of (12), one could employ Runge-Kutta-Nyström (RKN) methods, a special type of PRK methods developed for $\frac{d\mathbf{q}}{dt} = \mathbf{p}$, $\frac{d\mathbf{p}}{dt} = -\nabla V\left(\mathbf{q}\right)$, but in practice applicable to systems of the form (12) as well [50]. The RKN method of [51], for instance, is slightly more efficient than the method displayed in Table 1 [50]. However, as time-reversal symmetry was sacrificed for it, we did not opt for this method.

that the first step equals the last ($B_1 = B_5$), the second step the second-to-last ($b_1 = b_4$) and so on, the PRK method of Table 1 is symmetric. This way, time-reversal symmetry of the (2+1)D time-dependent Dirac equation is conserved.

Table 1: The coefficients of the optimised PRK method.

$$\begin{array}{cc} b_1 = \frac{6}{11} & B_1 = \frac{642+\sqrt{471}}{3924} \\ b_2 = -\frac{1}{22} & B_2 = \frac{121}{3924}\left(12-\sqrt{471}\right) \\ b_3 = b_2 & B_3 = 1 - 2B_1 - 2B_2 \\ b_4 = b_1 & B_4 = B_2 \\ b_5 = 0 & B_5 = B_1 \end{array}$$

To conclude this section, we instantiate the novel method by providing two update equations. For $\mathrm{Im}\,(\mathbf{u}_1)$, which is an element of $\mathbf{q}$, we get

$$\begin{aligned} \mathrm{Im}\,(U_1)|_{i,j}^{n,N} = \mathrm{Im}\,(U_1)|_{i,j}^{n,N-1} + \Delta t B_N \Bigg(& \frac{\left(-mc^2 - V_{u_1}|_{i,j}\right)}{\hbar} \mathrm{Re}\,(U_1)|_{i,j}^{n,N} \\ & - \frac{c}{24\Delta x}\left(-\mathrm{Im}\,(V_1)|_{i+1,j}^{n,N} + 27\mathrm{Im}\,(V_1)|_{i,j}^{n,N} - 27\mathrm{Im}\,(V_1)|_{i-1,j}^{n,N} + \mathrm{Im}\,(V_1)|_{i-2j,}^{n,N}\right) \\ & + \frac{c}{24\Delta y}\left(-\mathrm{Re}\,(V_2)|_{i,j+1}^{n,N} + 27\mathrm{Re}\,(V_2)|_{i,j}^{n,N} - 27\mathrm{Re}\,(V_2)|_{i,j-1}^{n,N} + \mathrm{Re}\,(V_2)|_{i,j-2}^{n,N}\right)\Bigg), \end{aligned} \tag{15}$$

where the capital letters refer to intermediate values, the index n to the time step and N to the substep. For $\mathrm{Re}\,(\mathbf{u}_1)$, which is an element of $\mathbf{p}$, we have

$$\begin{aligned} \mathrm{Re}\,(U_1)|_{i,j}^{n,N+1} = \mathrm{Re}\,(U_1)|_{i,j}^{n,N} + \Delta t b_N \Bigg(& \frac{\left(mc^2 + V_{u_1}|_{i,j}\right)}{\hbar} \mathrm{Im}\,(U_1)|_{i,j}^{n,N} \\ & - \frac{c}{24\Delta x}\left(-\mathrm{Re}\,(V_1)|_{i+1,j}^{n,N} + 27\mathrm{Re}\,(V_1)|_{i,j}^{n,N} - 27\mathrm{Re}\,(V_1)|_{i-1,j}^{n,N} + \mathrm{Re}\,(V_1)|_{i-2,j}^{n,N}\right) \\ & - \frac{c}{24\Delta y}\left(-\mathrm{Im}\,(V_2)|_{i,j+1}^{n,N} + 27\mathrm{Im}\,(V_2)|_{i,j}^{n,N} - 27\mathrm{Im}\,(V_2)|_{i,j-1}^{n,N} + \mathrm{Im}\,(V_2)|_{i,j-2}^{n,N}\right)\Bigg). \end{aligned} \tag{16}$$

The update equations for the other variables are similar.

5. Stability

In this section, we derive a stability criterion for the novel scheme, similar to the Courant–Friedrichs–Lewy condition. First, we make the observation that $\mathbf{K}\mathbf{K}^T$ is a normal matrix, and thus, it can be diagonalised by a unitary matrix as follows

$$\mathbf{\Lambda} = \mathbf{A}\mathbf{K}\mathbf{K}^T\mathbf{A}^\dagger, \tag{17}$$

with $\mathbf{A}$ being a unitary matrix, $\mathbf{A}^\dagger$ the Hermitian conjugate of $\mathbf{A}$ and $\mathbf{\Lambda}$ a diagonal matrix of which the diagonal elements correspond to the eigenvalues of $\mathbf{K}\mathbf{K}^T$. We left-multiply the first equation of (12) by $\mathbf{A}$ and the second equation by $\mathbf{A}\mathbf{K}$. Subsequently, we exploit the properties of unitary matrices and substitute $\mathbf{q}' = \mathbf{A}\mathbf{q}$ and $\mathbf{p}' = \mathbf{A}\mathbf{K}\mathbf{p}$ into the equations. This way, we obtain

$$\begin{aligned} \frac{\mathrm{d}\mathbf{q}'}{\mathrm{d}t} &= \mathbf{p}' \\ \frac{\mathrm{d}\mathbf{p}'}{\mathrm{d}t} &= -\mathbf{\Lambda}\mathbf{q}'. \end{aligned} \tag{18}$$

Owing to the diagonal nature of $\mathbf{\Lambda}$, the stability analysis of (12) has been simplified to investigating the stability of

$$\begin{aligned} \frac{\mathrm{d}q_l'}{\mathrm{d}t} &= p_l' \\ \frac{\mathrm{d}p_l'}{\mathrm{d}t} &= -\lambda_l q_l'. \end{aligned} \tag{19}$$

for $l = 1, ..., 4N_xN_y$, which is significantly less complicated. Adopting the PRK method of Section 4, results in a linear discrete-time system given by

$$\begin{pmatrix} q_l'^{n+1} \\ p_l'^{n+1} \end{pmatrix} = \boldsymbol{\mathcal{T}}(\lambda_l, 1) \begin{pmatrix} q_l'^{n} \\ p_l'^{n} \end{pmatrix}, \tag{20}$$

with amplification matrix

$$\boldsymbol{\mathcal{T}}(r, s) = \prod_{N=1}^{s} \begin{pmatrix} 1 & 0 \\ -\Delta t b_N r & 1 \end{pmatrix} \begin{pmatrix} 1 & \Delta t B_N s \\ 0 & 1 \end{pmatrix}, \tag{21}$$

which is an adapted version of the amplification matrix $\mathbf{T}$, defined in (14). The linear discrete-time system of (20) is Lyapunov stable if all eigenvalues of $\boldsymbol{\mathcal{T}}$ are located inside the unit circle or are semisimple when located on the unit circle [52]. For a general 2×2 matrix $\boldsymbol{\mathcal{T}}$ we get as eigenvalues

$$\frac{\mathrm{Tr}\,(\boldsymbol{\mathcal{T}}) \pm \sqrt{(\mathrm{Tr}\,(\boldsymbol{\mathcal{T}}))^2 - 4\mathrm{Det}\,(\boldsymbol{\mathcal{T}})}}{2}. \tag{22}$$

For $\boldsymbol{\mathcal{T}}$ given by (21), $\mathrm{Det}\,(\boldsymbol{\mathcal{T}}) = 1$. Hence, we must have that $|\mathrm{Tr}\,(\boldsymbol{\mathcal{T}})| \leq 2$ for the eigenvalues not to lay outside the unit circle. For $|\mathrm{Tr}\,(\boldsymbol{\mathcal{T}})| < 2$, we get two distinct, and thus semisimple eigenvalues. The case $|\mathrm{Tr}\,(\boldsymbol{\mathcal{T}})| = 2$ requires further attention. In this situation, (22) results in a single eigenvalue with an algebraic multiplicity of two, while the geometric multiplicity equals one. Consequently, the requirements for Lyapunov stability are not met in this case. We must continue with the condition $|\mathrm{Tr}\,(\boldsymbol{\mathcal{T}})| < 2$ for stability. The trace $\mathrm{Tr}\,(\boldsymbol{\mathcal{T}})$ is given by [45]

$$\mathrm{Tr}\,(\boldsymbol{\mathcal{T}}) = 2 + \sum_{N=1}^{s} (-1)^N g_N \left(\Delta t^2 \lambda_l\right)^N, \tag{23}$$

with

$$g_N = \sum_{1 \leq i_1 \leq j_1 < i_2 \leq j_2 < \ldots < i_N \leq j_N \leq s} B_{i_1} b_{j_1} B_{i_2} b_{j_2} \ldots B_{i_N} b_{j_N} + \sum_{1 \leq i_1 < j_1 \leq i_2 < j_2 \leq \ldots \leq i_N < j_N \leq s} b_{i_1} B_{j_1} b_{i_2} B_{j_2} \ldots b_{i_N} B_{j_N}. \tag{24}$$

This expression allows us to reduce $|\mathrm{Tr}\,(\boldsymbol{\mathcal{T}})| < 2$ to $\Delta t < C_{\mathrm{PRK}}/\sqrt{\lambda_l}$ as stability condition for (20), with C_{PRK} a constant determined by the PRK coefficients. Adopting the values of Table 1, C_{PRK} equals 3.0299. Stability of (12) requires stability of (20) for *all* eigenvalues λ_l of $\mathbf{K}\mathbf{K}^T$. Therefore, the stability condition for (12) is

$$\Delta t < \frac{C_{\mathrm{PRK}}}{\sqrt{\mathrm{max}_l\,(\lambda_l)}} = \frac{C_{\mathrm{PRK}}}{\sqrt{\rho\,(\mathbf{K}\mathbf{K}^T)}}, \tag{25}$$

with $\rho\left(\mathbf{K}\mathbf{K}^T\right)$ the spectral radius of $\mathbf{K}\mathbf{K}^T$.

Numerically calculating this spectral radius is a computationally expensive operation and becomes intractable in practical application of the novel method to simulate (2+1)D Dirac problems. Therefore, we follow the approach of [53] and make an estimate of the spectral radius yielding a "Courant–Friedrichs–Lewy-like" condition. The spectral radius is bounded by any induced norm, for instance by the infinity norm:

$$\rho\left(\mathbf{K}\mathbf{K}^T\right) \leq \|\mathbf{K}\mathbf{K}^T\|_\infty = \max_i \sum_{j=1} |[\mathbf{K}\mathbf{K}^T]_{i,j}|. \tag{26}$$

Applying this estimate finally yields an easy-to-handle stability condition for the time step:

$$\Delta t < \frac{C_{\mathrm{PRK}}}{\sqrt{\mathrm{max}_i \left(\frac{\left(mc^2 \pm [\mathbf{V}]_{i,i}\right)^2}{\hbar^2} + \left(\frac{7c}{3}\right)^2 \left(\frac{1}{\Delta x^2} + \frac{1}{\Delta y^2}\right) + \frac{14c}{3\hbar} |[\mathbf{V}]_{i,i}| \left(\frac{1}{\Delta x} + \frac{1}{\Delta y}\right) \right)}}, \tag{27}$$

where $\mathbf{V}$ accounts for $\mathbf{V}_{\mathbf{u}_1}$, $\mathbf{V}_{\mathbf{u}_2}$, $\mathbf{V}_{\mathbf{v}_1}$ and $\mathbf{V}_{\mathbf{v}_2}$.

6. Dispersion

Besides stability, the numerical dispersion of the novel scheme also needs to be investigated. Thereto, we adopt a complex frequency analysis to retrieve a numerical analogue of the continuous dispersion relation for a free massless particle, i.e., $\omega = \pm kc$ (or $E = \pm pc$), which corresponds to the plane wave solution

$$\mathbf{\Psi}(x,y,t) = \begin{pmatrix} u(x,y,t) \\ v(x,y,t) \end{pmatrix} = \begin{pmatrix} U \\ V \end{pmatrix} \exp\left(\imath k_x x + \imath k_y y - \imath\omega t\right), \tag{28}$$

where $k = \sqrt{k_x^2 + k_y^2}$. As a first step, the discretisation of the plane wave is put forward, yielding the following expressions for the components of $\mathbf{q}$ and $\mathbf{p}$, of which the spatial part is fully detailed:

$$\begin{aligned}
\mathrm{Im}\,(U_1)|_{i,j}^{n,N} &= \mathrm{Im}\left(\tilde{U}\right)|^{n,N} \exp\left(\imath k_x i\Delta x + \imath k_y j\Delta y\right) \\
\mathrm{Re}\,(U_2)|_{i,j}^{n,N} &= \mathrm{Re}\left(\tilde{U}\right)|^{n,N} \exp\left(\imath k_x (i+1/2)\Delta x + \imath k_y (j+1/2)\Delta y\right) \\
\mathrm{Re}\,(V_1)|_{i,j}^{n,N} &= \mathrm{Re}\left(\tilde{V}\right)|^{n,N} \exp\left(\imath k_x (i+1/2)\Delta x + \imath k_y j\Delta y\right) \\
\mathrm{Im}\,(V_2)|_{i,j}^{n,N} &= \mathrm{Im}\left(\tilde{V}\right)|^{n,N} \exp\left(\imath k_x i\Delta x + \imath k_y (j+1/2)\Delta y\right) \\
\mathrm{Re}\,(U_1)|_{i,j}^{n,N} &= \mathrm{Re}\left(\hat{U}\right)|^{n,N} \exp\left(\imath k_x i\Delta x + \imath k_y j\Delta y\right) \\
\mathrm{Im}\,(U_2)|_{i,j}^{n,N} &= \mathrm{Im}\left(\hat{U}\right)|^{n,N} \exp\left(\imath k_x (i+1/2)\Delta x + \imath k_y (j+1/2)\Delta y\right) \\
\mathrm{Im}\,(V_1)|_{i,j}^{n,N} &= \mathrm{Im}\left(\hat{V}\right)|^{n,N} \exp\left(\imath k_x (i+1/2)\Delta x + \imath k_y j\Delta y\right) \\
\mathrm{Re}\,(V_2)|_{i,j}^{n,N} &= \mathrm{Re}\left(\hat{V}\right)|^{n,N} \exp\left(\imath k_x i\Delta x + \imath k_y (j+1/2)\Delta y\right),
\end{aligned} \tag{29}$$

where indices i and j refer to the spatial grid of Fig. 1 and where n and N are the indices indicating the main time step and the substep. Note that variables related to $\mathbf{q}$ and $\mathbf{p}$ are denoted by a tilde and a hat, respectively. Second, we substitute (29) into the update equations (such as (15) and (16)) and obtain

$$\begin{aligned}
\tilde{U}|^{n,N} &= \tilde{U}|^{n,N-1} + \Delta t B_N D \hat{V}|^{n,N} \\
\tilde{V}|^{n,N} &= \tilde{V}|^{n,N-1} - \Delta t B_N D^* \hat{V}|^{n,N} \\
\hat{U}|^{n,N+1} &= \left(1 - \Delta t^2 B_N b_N |D|^2\right) \hat{U}|^{n,N} + \Delta t b_N D \tilde{V}|^{n,N-1} \\
\hat{V}|^{n,N+1} &= \left(1 - \Delta t^2 B_N b_N |D|^2\right) \hat{V}|^{n,N} - \Delta t b_N D^* \tilde{U}|^{n,N-1},
\end{aligned} \tag{30}$$

with

$$D = -\frac{\imath c}{12\Delta x}\left[-\sin\left(\frac{3}{2}k_x\Delta x\right) + 27\sin\left(\frac{1}{2}k_x\Delta x\right)\right] - \frac{c}{12\Delta y}\left[-\sin\left(\frac{3}{2}k_y\Delta y\right) + 27\sin\left(\frac{1}{2}k_y\Delta y\right)\right]. \tag{31}$$

In (30), the real and imaginary parts of each variable have been concatenated again, while D contains all information about the spatial derivatives. As one notes that $\tilde{U}$ and $\hat{V}$ are completely decoupled from $\tilde{V}$ and $\hat{U}$, we may proceed with the first and last equation of (30). The second and third equation return similar results. Successive application of the s substeps yields

$$\begin{pmatrix} \tilde{U}|^{n+1,0} \\ \hat{V}|^{n+1,1} \end{pmatrix} = \boldsymbol{\mathcal{T}}(D^*, D) \begin{pmatrix} \tilde{U}|^{n,0} \\ \hat{V}|^{n,1} \end{pmatrix}, \tag{32}$$

with $\boldsymbol{\mathcal{T}}$ the amplification matrix given by (21). Third, substitution of the temporal part of the plane wave expression

$$\begin{aligned}
\tilde{U}|^{n,0} &= \tilde{\tilde{U}} \exp\left(-\imath\omega n\Delta t\right) \\
\hat{V}|^{n,1} &= \hat{\tilde{U}} \exp\left(-\imath\omega n\Delta t\right)
\end{aligned} \tag{33}$$

into (32), yields

$$\exp\left(-\imath\omega\Delta t\right) \begin{pmatrix} \tilde{\tilde{U}} \\ \hat{\tilde{V}} \end{pmatrix} = \boldsymbol{\mathcal{T}}(D^*, D) \begin{pmatrix} \tilde{\tilde{U}} \\ \hat{\tilde{V}} \end{pmatrix}. \tag{34}$$

Finally, we get the numerical dispersion relation

$$\omega_{\text{num}} = \frac{\imath}{\Delta t} \ln\left(\lambda_{\pm}\left(\mathcal{T}(D^*, D)\right)\right), \tag{35}$$

with $\lambda_{\pm}\left(\mathcal{T}(D^*, D)\right)$ the two eigenvalues of $\mathcal{T}(D^*, D)$. Therefore, (35) corresponds to two equations similar as one gets in the continuous case, i.e., $\omega_{\text{cont}} = \pm kc$. Based on the ideas of Section 5, it is readily shown that these eigenvalues of $\mathcal{T}(D^*, D)$ are situated on the unit circle when the time step satisfies (27). Consequently, $\text{Im}\left(\omega_{\text{num}}\right)$ is zero and no additional dissipation is introduced via PRK time stepping in contrast to the RK time stepping of Section 3.

The rationale behind this paper is to construct a novel higher-order method for the (2+1)D time-dependent Dirac equation, which, besides exhibiting excellent conservation properties (see Section 7), also avoids the large dispersion errors of second-order accurate schemes. As an illustration of this advantage of our higher-order method, we compare the relative error on the numerical dispersion relation, defined by $E_{\omega,\text{Re}} = \frac{|\omega_{\text{cont}} - \text{Re}(\omega_{\text{num}})|}{\omega_{\text{cont}}}$, between the second-order leapfrog method of [29], the RK4 based method (Appendix A) and the novel scheme as a function of the number of gridsteps per wavelength and as a function of ϕ, viz. the angle between the wave vector and the x-axis. The results are shown in Fig. 3, where $\Delta x = \Delta y$ and with Δt as large as possible but still satisfying the relevant stability condition. For the novel scheme, Δt is determined by (27) and for the RK4 based method by (A.8). We employ

$$\Delta t \leq \frac{1}{c\sqrt{\frac{1}{\Delta x^2} + \frac{1}{\Delta y^2}}} \tag{36}$$

for the leapfrog method, which is also valid for massive particles and non-zero scalar potential [29]. The higher-order methods are considerably more accurate for the same number of gridsteps per wavelength than the leapfrog method and display the expected fourth-order behaviour. Furthermore, the error of the PRK based method is lower than the error of the method leveraging RK4. Fig. 3b compares the magnitude of the anisotropy of the three schemes. As the dispersion relation of the leapfrog method approaches asymptotically the continuous relation in the neighbourhood of $\phi = \frac{\pi}{4} + m\frac{\pi}{2}$ ($m \in \mathbb{N}$), it suffers considerably from anisotropy, whereas for the higher-order methods anisotropy is far less pronounced.

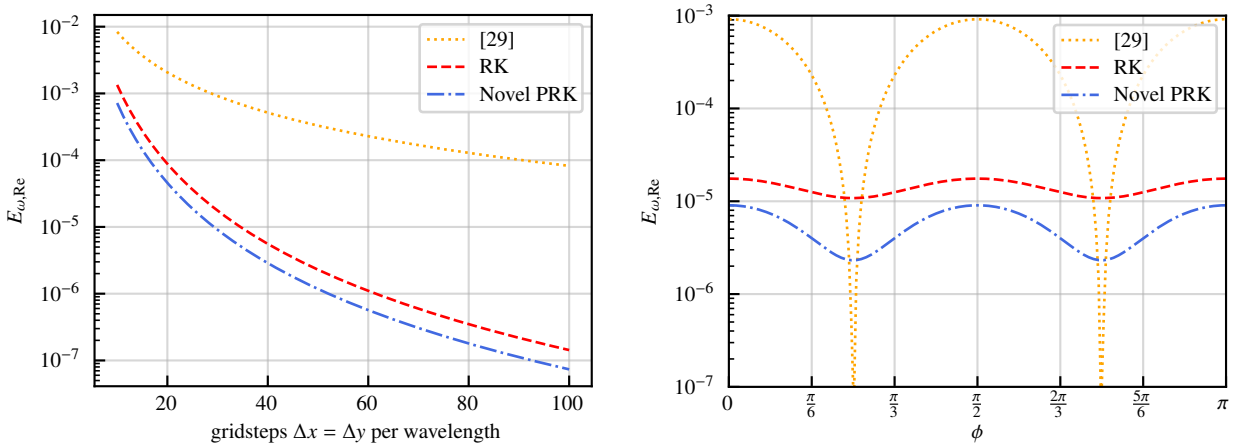

(a) Relative error on the real part of the numerical frequency $E_{\omega,\text{Re}}$ as a function of the number of gridsteps per wavelength for $\phi = 0$.

(b) Relative error on the real part of the numerical frequency $E_{\omega,\text{Re}}$ as a function of ϕ for 30 gridsteps per wavelength.

Figure 3: Comparison of the dispersion error as function of (a) the number of gridsteps per wavelength and (b) ϕ, between the leapfrog method of [29] and the higher-order methods based on RK and PRK time stepping.

7. Conservation laws

In this section, we examine some fundamental geometric properties of the novel numerical scheme. We will start with symplecticness. Symplectic time evolution operators are intimately related to Hamiltonian systems, as the relation works either way, i.e., Hamiltonian systems have a symplectic time evolution operator and, oppositely, a symplectic time evolution operator implies that the system must be Hamiltonian [40]. One can easily proof by contradiction that the coupled ODEs (12), obtained after careful spatial discretisation of the (2+1)D Dirac equation, do not correspond to a Hamiltonian system for the particular choice of $\mathbf{q}$ and $\mathbf{p}$. Consequently, one could question the usefulness of a symplectic time integrator. However, symplecticness of the time stepping scheme implies non-dissipativeness [54], already avoiding the problems related to the RK methods illustrated in Fig. 2. Moreover, we can make the case for applying a symplectic PRK method to (12) even stronger. Thereto, consider

$$\frac{\mathrm{d}\mathbf{y}}{\mathrm{d}t} = \boldsymbol{\mathcal{B}}\,\nabla H\left(\mathbf{y}\right), \tag{37}$$

with $\boldsymbol{\mathcal{B}}$ a constant matrix. The set of ODEs (37) is called a Poisson system [36] under the condition

$$\left[\boldsymbol{\mathcal{B}}\right]_{i,j} = -\left[\boldsymbol{\mathcal{B}}\right]_{j,i}. \tag{38}$$

When taking $\boldsymbol{\mathcal{B}} = \left(\begin{smallmatrix} 0 & \mathbf{K} \\ -\mathbf{K}^T & 0 \end{smallmatrix}\right)$ and $H = 1/2\,\mathbf{q}^T\mathbf{q} + 1/2\,\mathbf{p}^T\mathbf{p}$, (12) is recast as a Poisson system (37), where condition (38) is trivially satisfied. Similar to Hamiltonian systems, the time evolution operator of (37) is characterised by a fundamental geometric property, being a Poisson map. A linear map $\boldsymbol{\Phi} : \mathbb{R}^{2d} \mapsto \mathbb{R}^{2d} : \mathbf{y} \mapsto \mathbf{A}\mathbf{y}$, with $\mathbf{A} \in \mathbb{R}^{2d\times 2d}$ and $2d$ the dimension of $\mathbf{y}$, is a Poisson map with respect to matrix $\boldsymbol{\mathcal{B}}$ if $\mathbf{A}$ satisfies

$$\mathbf{A}^T\boldsymbol{\mathcal{B}}\,\mathbf{A} = \boldsymbol{\mathcal{B}}. \tag{39}$$

Note that a Hamiltonian system is a particular type of Poisson system. We now demonstrate that the PRK scheme corresponds to a Poisson map with respect to $\boldsymbol{\mathcal{B}} = \left(\begin{smallmatrix} 0 & \mathbf{K} \\ -\mathbf{K}^T & 0 \end{smallmatrix}\right)$. Thereto, the matrix

$$\mathbf{T}^T\boldsymbol{\mathcal{B}}\,\mathbf{T} = \left(\prod_{N=1}^{s}\begin{pmatrix} 1 & 0 \\ -\Delta t b_N\mathbf{K}^T & 1 \end{pmatrix}\begin{pmatrix} 1 & \Delta t B_N\mathbf{K} \\ 0 & 1 \end{pmatrix}\right)^T \boldsymbol{\mathcal{B}} \left(\prod_{N=1}^{s}\begin{pmatrix} 1 & 0 \\ -\Delta t b_N\mathbf{K}^T & 1 \end{pmatrix}\begin{pmatrix} 1 & \Delta t B_N\mathbf{K} \\ 0 & 1 \end{pmatrix}\right), \tag{40}$$

with $\mathbf{T}$ the amplification matrix of the PRK scheme, which was introduced in (14), should equal $\boldsymbol{\mathcal{B}}$. It suffices to study

$$\begin{pmatrix} 1 & 0 \\ \Delta t B_N\mathbf{K}^T & 1 \end{pmatrix}\begin{pmatrix} 1 & -\Delta t b_N\mathbf{K} \\ 0 & 1 \end{pmatrix} \boldsymbol{\mathcal{B}} \begin{pmatrix} 1 & 0 \\ -\Delta t b_N\mathbf{K}^T & 1 \end{pmatrix}\begin{pmatrix} 1 & \Delta t B_N\mathbf{K} \\ 0 & 1 \end{pmatrix}, \tag{41}$$

of which it is easily shown that it equals $\boldsymbol{\mathcal{B}}$ for all $N = 1, ..., s$. As a result, the PRK method conserves the Poisson property of the time evolution operator, making it a Poisson integrator.

We exploit the property of the PRK method being a Poisson integrator with respect to $\boldsymbol{\mathcal{B}} = \left(\begin{smallmatrix} 0 & \mathbf{K} \\ -\mathbf{K}^T & 0 \end{smallmatrix}\right)$ and $H = 1/2\,\mathbf{q}^T\mathbf{q} + 1/2\,\mathbf{p}^T\mathbf{p}$ to investigate the conservation of probability. The analysis is based on the ideas of backward error interpretation from [36, 40]. To solve a system like (37), we approximate the time evolution operator by a numerical method, which produces after each time step the values $\mathbf{y}|^0, \mathbf{y}|^1, \mathbf{y}|^2, ...$ In a forward error analysis, these values are compared to exact solutions and an assessment of the error is made in solution space. In backward error analysis, we search for a modified differential equation of which the time evolution operator is exactly equal to the one related to the numerical method applied on the original system and thus, of which $\mathbf{y}|^0, \mathbf{y}|^1, \mathbf{y}|^2, ...$ are the exact solutions. By investigating this modified differential equation, one can obtain additional insights into the behaviour of the numerical method. When applying a Poisson time integrator of order m to the original Poisson system (37), we get — under the conditions of $H\left(\mathbf{y}\right)$ being smooth and $\boldsymbol{\mathcal{B}}$ being invertible — the following modified differential equation

$$\frac{\mathrm{d}\mathbf{y}}{\mathrm{d}t} = \boldsymbol{\mathcal{B}}\left(\nabla H\left(\mathbf{y}\right) + \Delta t^m \nabla H_m\left(\mathbf{y}\right) + \Delta t^{m+1}\nabla H_{m+1}\left(\mathbf{y}\right) + ...\right), \tag{42}$$

where $H_j\left(\mathbf{y}\right)$ with $j = m, m+1, ...$ are smooth functions. Hence, the modified differential equation of a Poisson integrator applied to a Poisson system is again a Poisson system. Poisson systems of the form (37) conserve $H\left(\mathbf{y}\right)$

exactly. Accordingly, the time evolution operator of (42) conserves $H(\mathbf{y}) + \Delta t^m H_m(\mathbf{y}) + \Delta t^{m+1} H_{m+1}(\mathbf{y}) + ...$ As the numerical integrator coincides with the time evolution operator of the modified differential equation, it also conserves $H(\mathbf{y}) + \Delta t^m H_m(\mathbf{y}) + \Delta t^{m+1} H_{m+1}(\mathbf{y}) + ...$ exactly (instead of conserving $H(\mathbf{y})$). In our particular case, H is proportional to the total probability $\mathcal{P}$ (7) and, hence, the numerical integrator conserves a slightly different expression, which deviates from the true expression by terms only starting from Δt^4. Moreover, the error term $\Delta t^4 H_4(\mathbf{y}) + \Delta t^5 H_5(\mathbf{y}) + ...$ does not scale with the total duration t or thus the total number of time steps n. Consequently, the total probability will not drift away, in contrast to the RK method (see Fig. 2a).

Similarly, we study the conservation of the total energy. We start from the continuous expression

$$\int_{-\infty}^{+\infty}\int_{-\infty}^{+\infty} u^*\left(-\imath\hbar c\left(\frac{\partial}{\partial x}-\imath\frac{\partial}{\partial y}\right)v+\left(mc^2+V\right)u\right)+v^*\left(-\imath\hbar c\left(\frac{\partial}{\partial x}+\imath\frac{\partial}{\partial y}\right)u+\left(-mc^2+V\right)v\right)\mathrm{d}x\,\mathrm{d}y \tag{43}$$

and approximate it by its fourth-order accurate spatially discretised equivalent

$$\mathcal{E} = \frac{\Delta x\,\Delta y}{2}\mathbf{q}^T\mathbf{E}_q\mathbf{q} + \frac{\Delta x\,\Delta y}{2}\mathbf{p}^T\mathbf{E}_p\mathbf{p}, \tag{44}$$

with

$$\mathbf{E_q} = \begin{pmatrix} mc^2+\mathbf{V}_{\mathbf{u}_1} & 0 & -\hbar c\mathbf{D}_{4,x} & -\hbar c\mathbf{D}_{4,y} \\ 0 & mc^2+\mathbf{V}_{\mathbf{u}_2} & \hbar c\mathbf{D}_{4,y}^T & -\hbar c\mathbf{D}_{4,x}^T \\ -\hbar c\mathbf{D}_{4,x}^T & \hbar c\mathbf{D}_{4,y} & -mc^2+\mathbf{V}_{\mathbf{v}_1} & 0 \\ -\hbar c\mathbf{D}_{4,y}^T & -\hbar c\mathbf{D}_{4,x} & 0 & -mc^2+\mathbf{V}_{\mathbf{v}_2} \end{pmatrix} \tag{45}$$

and

$$\mathbf{E_p} = \begin{pmatrix} mc^2+\mathbf{V}_{\mathbf{u}_1} & 0 & \hbar c\mathbf{D}_{4,x} & -\hbar c\mathbf{D}_{4,y} \\ 0 & mc^2+\mathbf{V}_{\mathbf{u}_2} & \hbar c\mathbf{D}_{4,y}^T & \hbar c\mathbf{D}_{4,x}^T \\ \hbar c\mathbf{D}_{4,x}^T & \hbar c\mathbf{D}_{4,y} & -mc^2+\mathbf{V}_{\mathbf{v}_1} & 0 \\ -\hbar c\mathbf{D}_{4,y}^T & \hbar c\mathbf{D}_{4,x} & 0 & -mc^2+\mathbf{V}_{\mathbf{v}_2} \end{pmatrix}. \tag{46}$$

We repeat the previous analysis but instead of choosing $\mathcal{B} = \left(\begin{smallmatrix} 0 & \mathbf{K} \\ -\mathbf{K}^T & 0 \end{smallmatrix}\right)$ and $H = 1/2\,\mathbf{q}^T\mathbf{q} + 1/2\,\mathbf{p}^T\mathbf{p}$, we opt for $\mathcal{B} = \left(\begin{smallmatrix} 0 & \mathbf{D} \\ -\mathbf{D} & 0 \end{smallmatrix}\right)$, with

$$\mathbf{D} = \frac{1}{\hbar}\begin{pmatrix} -\mathbf{I}_{N_xN_y} & 0 & 0 & 0 \\ 0 & \mathbf{I}_{N_xN_y} & 0 & 0 \\ 0 & 0 & \mathbf{I}_{N_xN_y} & 0 \\ 0 & 0 & 0 & -\mathbf{I}_{N_xN_y} \end{pmatrix} \tag{47}$$

and $H = 1/2\,\mathbf{q}^T\mathbf{E}_q\mathbf{q} + 1/2\,\mathbf{p}^T\mathbf{E}_p\mathbf{p}$. Note that H is now proportional to the total energy $\mathcal{E}$ (44). With this new definition of $\mathcal{B}$ and H, (12) is again recast as a Poisson system (37) and thus, following the same approach as for the total probability, we can demonstrate theoretically that the PRK method conserves the total energy approximately, i.e., it conserves a modified expression of the total energy which deviates from the true expression only by an error term which is of the fourth order of the time step.

For momentum, which is only a constant of motion when the potential V is independent of the position, we follow a different approach. We start from the continuous expression of the total momentum in the x-direction

$$\int_{-\infty}^{+\infty}\int_{-\infty}^{+\infty} u^*\left(-\imath\hbar\frac{\partial}{\partial x}\right)u + v^*\left(-\imath\hbar\frac{\partial}{\partial x}\right)v\,\mathrm{d}x\,\mathrm{d}y \tag{48}$$

and approximate it by its fourth-order accurate spatially discretised equivalent $\mathcal{M}_x = \mathbf{p}^T\mathbf{M}_x\mathbf{q}$, with

$$\mathbf{M}_x = \hbar\,\Delta x\,\Delta y\begin{bmatrix} \mathbf{D}'_{4,x} & 0 & 0 & 0 \\ 0 & -\mathbf{D}'_{4,x} & 0 & 0 \\ 0 & 0 & -\mathbf{D}'_{4,x} & 0 \\ 0 & 0 & 0 & \mathbf{D}'_{4,x} \end{bmatrix}, \tag{49}$$

$$\mathbf{D}'_{4,x} = \mathbf{d}'_{4,x} \otimes \mathbf{I}_{N_y}, \tag{50}$$

$$[\mathbf{d}'_{4,x}]_{i,j} = \frac{1}{12\Delta x}\left(\delta_{i,j-2} - 8\delta_{i,j-1} + 8\delta_{i,j+1} - \delta_{i,j+2}\right). \tag{51}$$

A similar discretisation can be made for the total momentum in the y-direction. Generally, if $I(\mathbf{p}, \mathbf{q}) = \mathbf{p}^T\mathbf{A}\mathbf{q}$, with $\mathbf{A}$ a constant matrix, is a conserved quantity of (8), then I is also conserved when the system is integrated by an explicit symplectic PRK method [36, 40]. Consequently, the total momentum along the x- or y-direction is *exactly* conserved by our advocated method.

We conclude this section about the conservation laws with a numerical test, which is the same as the test in Section 3. The results are shown in Fig. 4. In accordance with the expectations, the relative error on the total momentum $E_{\mathcal{M}}(n) = \frac{|\mathcal{M}(n)-\mathcal{M}(0)|}{|\mathcal{M}(0)|}$ is situated near machine precision. The relative error on both the total probability $E_{\mathcal{P}}(n) = \frac{|\mathcal{P}(n)-\mathcal{P}(0)|}{|\mathcal{P}(0)|}$ and the total energy $E_{\mathcal{E}}(n) = \frac{|\mathcal{E}(n)-\mathcal{E}(0)|}{|\mathcal{E}(0)|}$ oscillates about a very small value, which agrees with the analytical predictions as well. In practical examples, this error will be negligible.

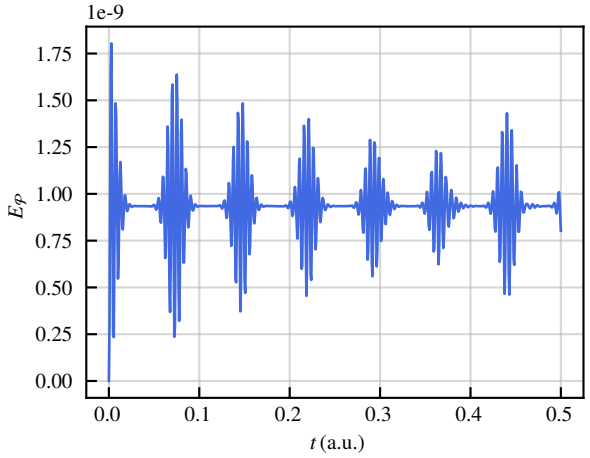

(a) Evolution of the relative error on the total probability $\mathcal{P}$ over time.

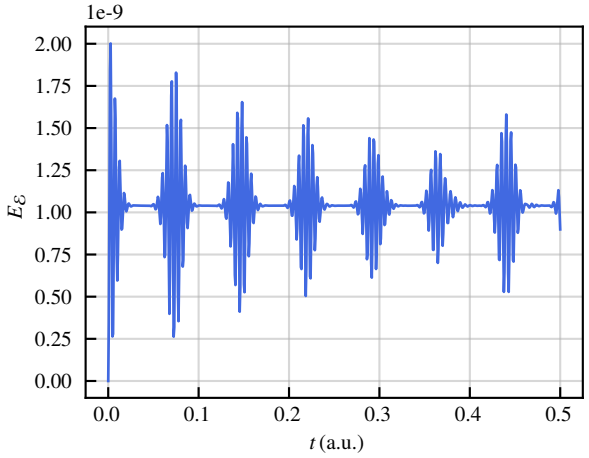

(b) Evolution of the relative error on the total energy $\mathcal{E}$ over time.

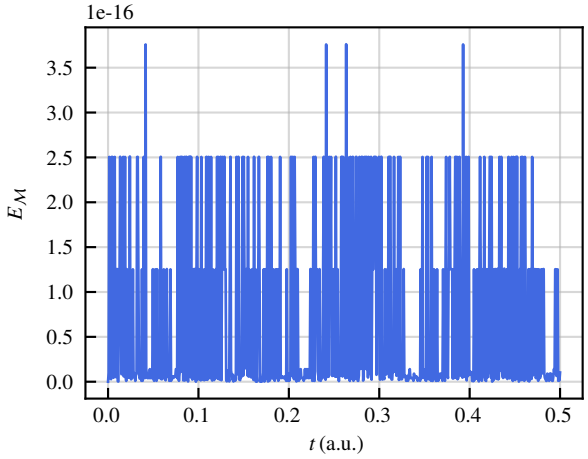

(c) Evolution of the relative error on the total momentum $\mathcal{M}$ over time.

Figure 4: Illustration of the conservation properties of the novel scheme. As parameters, expressed in a.u., for the initial wave function (5), we take $m = 0$, $x_0 = y_0 = 0$, $p_{x,0} = 4$, $p_{y,0} = 0$ and $\sigma_x = \sigma_y = 1$. The simulation domain ranges from -10 to 10 in both the x- and y-direction, while both N_x and N_y are equal to 200, leading to a spatial step $\Delta x = \Delta y = 0.1$. The corresponding time step Δt, determined by the stability condition (27), is $6.702\,10^{-4}$, resulting in 747 steps.

8. Numerical validation

In this section, we present several interesting numerical simulation results. Besides validating the novel PRK inspired method, they also illustrate its advantages compared to the scheme based on RK4, described in Appendix A, and the leapfrog method of [29]. To guarantee a fair comparison, all numerical schemes are implemented in Python employing the NumPy-package [55] and are optimised for speed. Thereto, in all update equations (e.g., (15) and (16) for the PRK method) time-independent variables are calculated only once and stored during the setup phase of the simulation, thereby reducing the number of floating point operations at every time step. However, in doing so, memory consumption is increased. The numerical simulations are all performed on a Dell laptop with Intel Core i7 Processor (6×2.70 GHz) and 16 GB RAM. Additionally, remark that in every simulation example the momentum of the initial wavefunction is chosen to be close to the Dirac cone of the continuous dispersion relation. This way, the fermion doubling problem does not pose any issues.

As a first simulation example, we consider the propagation of a free particle. This simple situation is one of the few problems for which an analytical solution can be found. This reference solution is easily determined up to a high accuracy without any additional approximation and it is thus perfectly suited for a thorough analysis of the efficiency of the numerical methods. The derivation of the analytical solution follows the same approach as [26]. We choose the gaussian wavepacket of (5) as initial wave function and transform it to momentum space

$$\begin{aligned}\hat{\boldsymbol{\Psi}}\left(0,p_x,p_y\right) = 4\pi N\sigma_x\sigma_y\begin{pmatrix}1\\C\end{pmatrix}\exp\left(-\sigma_x^2\left(\frac{p_x-p_{x,0}}{\hbar}\right)^2\right)\exp\left(-\sigma_y^2\left(\frac{p_y-p_{y,0}}{\hbar}\right)^2\right)\\ \exp\left(-\imath\left(\frac{p_x-p_{x,0}}{\hbar}\right)x_0\right)\exp\left(-\imath\left(\frac{p_y-p_{y,0}}{\hbar}\right)y_0\right).\end{aligned} \tag{52}$$

In momentum space, the time propagation operator for a free particle is readily determined, leading to the wave function at time instance t:

$$\hat{\boldsymbol{\Psi}}\left(t,p_x,p_y\right) = \left[\begin{pmatrix}1&0\\0&1\end{pmatrix}\cos\left(\frac{E}{\hbar}t\right) - \frac{\imath}{E}\left(\begin{pmatrix}0&1\\1&0\end{pmatrix}p_xc + \begin{pmatrix}0&-\imath\\\imath&0\end{pmatrix}p_yc + \begin{pmatrix}1&0\\0&-1\end{pmatrix}mc^2\right)\sin\left(\frac{E}{\hbar}t\right)\right]\hat{\boldsymbol{\Psi}}\left(0,p_x,p_y\right). \tag{53}$$

As final step, we transform back to real space via

$$\boldsymbol{\Psi}\left(t,x,y\right) = \frac{1}{(2\pi\hbar)^2}\int_{-\infty}^{+\infty}\int_{-\infty}^{+\infty}\hat{\boldsymbol{\Psi}}\left(t,p_x,p_y\right)\exp\left(\imath\frac{p_x}{\hbar}x\right)\exp\left(\imath\frac{p_y}{\hbar}y\right)\mathrm{d}p_x\mathrm{d}p_y. \tag{54}$$

To evaluate the integrals in (54), a specialised routine of the SciPy-package [56] is invoked. A high precision is achieved this way, which allows us to accurately quantitatively analyse the performance of the advocated scheme and compare it with other numerical methods. Evaluating double integrals of the type (54) for all points on a 2D grid is, however, a time consuming task. Therefore, we restrict ourselves to comparing the analytical and numerical solution for component u of $\boldsymbol{\Psi}$ at the position where the probability density $\boldsymbol{\Psi}^\dagger\boldsymbol{\Psi}$ reaches its maximum when the simulation is stopped. The relative error, here defined by $E_u = \frac{|u_{\mathrm{ana}}-u_{\mathrm{num}}|}{|u_{\mathrm{ana}}|}$, is again employed as the figure of merit.

A first set of results is displayed in Fig. 5, where we study the particular situation of a massless particle propagating along the x-direction ($p_{x,0} = 4$; $p_{y,0} = 0$) and a massless particle propagating along the diagonal ($p_{x,0} = p_{y,0} = 2\sqrt{2}$). In both cases, the total momentum of the particle is centred around 4. The simulation is stopped after t=0.04 to prevent that the particle reaches the edges of the domain and is disturbed by the periodic boundary condition. For all three numerical methods, the time step is determined by the relevant stability condition ((36) for [29], (A.8) for RK and (27) for our novel PRK). Fig. 5a illustrates the order of accuracy of the numerical methods. As expected, the relative error for the novel fourth-order accurate PRK inspired scheme scales with Δx^4. The other two methods also exhibit the expected behaviour. Note that the PRK scheme performs better than the RK scheme. The relative error as a function of the spatial step for propagation along the diagonal is shown in Fig. 5b. As expected from the dispersion relation and Fig. 3b, the leapfrog method is significantly more accurate in this case than for propagation along the x-axis, again illustrating the anisotropy related to this method. For our scheme, only a limited amount of anisotropy is observed.

Besides studying the accuracy of the numerical method as a function of the spatial step, we also take the total simulation time into account to investigate the efficiency. Fig. 5c shows the total simulation time required to reach a certain

accuracy for a massless particle travelling along the x-axis. The novel PRK scheme is more efficient than the scheme of [29] starting already from an accuracy slightly below 0.1. Remark that this cross-over point corresponds to a spatial step $\Delta x \approx 0.1$ for the leapfrog method (see Fig. 5a). We approximate the maximal momentum along the x-axis of the gaussian wave packet (5) by $p_{x,0} + 2/\sigma_x$, leading to a minimum de Broglie wavelength of 1.047. Consequently, the cross-over point corresponds to only about ten steps per wavelength. To put this in perspective, in electromagnetic FDTD simulations typically twenty steps per wavelength are used [57]. Similar observations are obtained from Fig. 5d for a particle propagating along the diagonal, where due to the large anisotropy the leapfrog method seems to perform somewhat better.

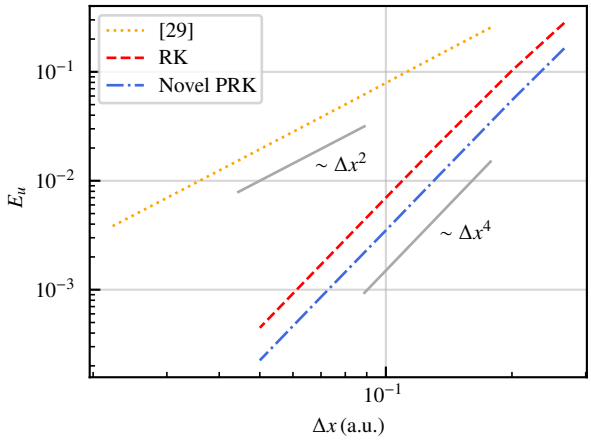

(a) Relative error as a function of the spatial step for a particle travelling along the x-direction, i.e., $p_{x,0} = 4$ and $p_{y,0} = 0$. Trendlines are shown in grey.

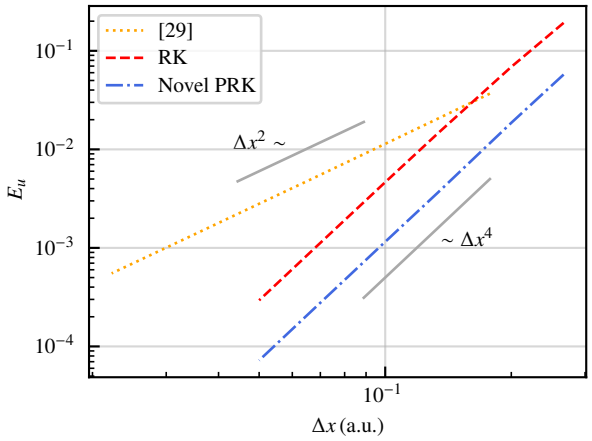

(b) Relative error as a function of the spatial step for a particle travelling along the diagonal, i.e., $p_{x,0} = p_{y,0} = 2\sqrt{2}$. Trendlines are shown in grey.

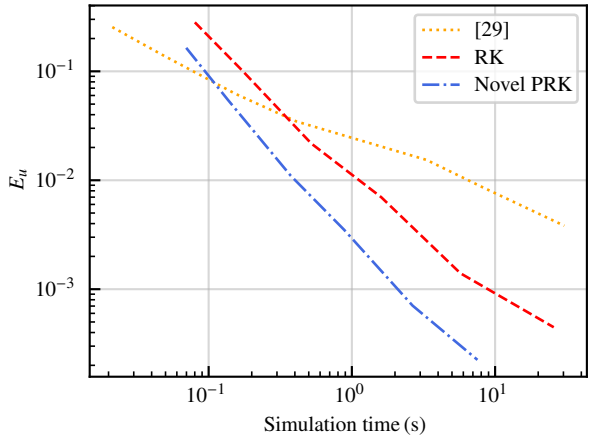

(c) Relative error as a function of the total simulation time for a particle travelling along the x-direction, i.e., $p_{x,0} = 4$ and $p_{y,0} = 0$. The indicated relative error E_u is obtained by adjusting the spatial step size.

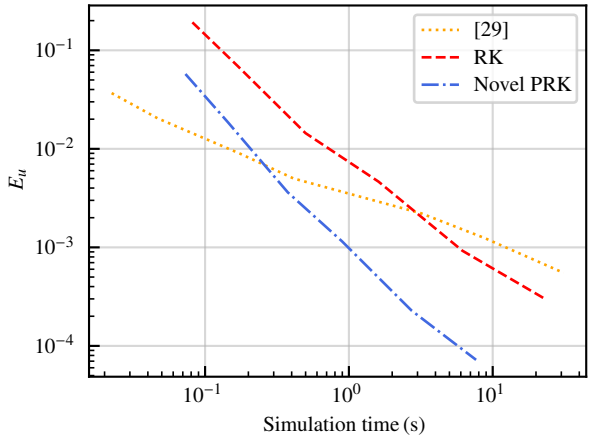

(d) Relative error as a function of the total simulation time for a particle travelling along the diagonal, i.e., $p_{x,0} = p_{y,0} = 2\sqrt{2}$. The indicated relative error E_u is obtained by adjusting the spatial step size.

Figure 5: Quantitative comparison between the novel PRK method, the RK method and the scheme of [29] for a massless free particle with total momentum centred around four. The remaining parameters of the initial wave function (5) are given by $x_0 = y_0 = 0$ and $\sigma_x = \sigma_y = 1$. The simulation domain ranges from -8 to 8 in both x- and y-direction. The particle is propagated over 0.04. All quantum mechanical quantities are expressed in atomic units. The spatial steps are always chosen equal ($\Delta x = \Delta y$) while the time step is determined by the relevant stability condition as indicated in the text.

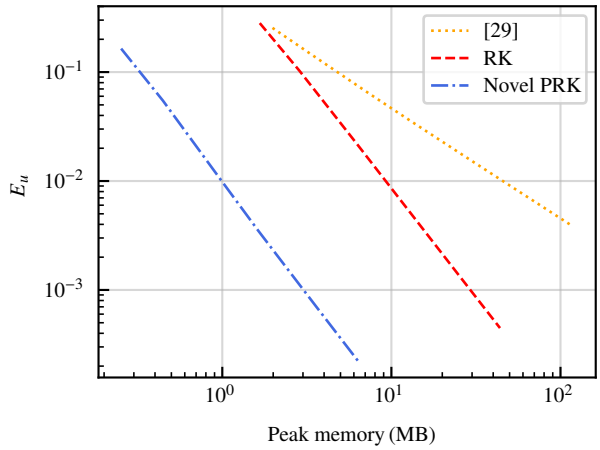

(e) Relative error as a function of peak memory consumption for a particle travelling along the x-direction, i.e., $p_{x,0} = 4$ and $p_{y,0} = 0$. The indicated relative error E_u is obtained by adjusting the spatial step size.

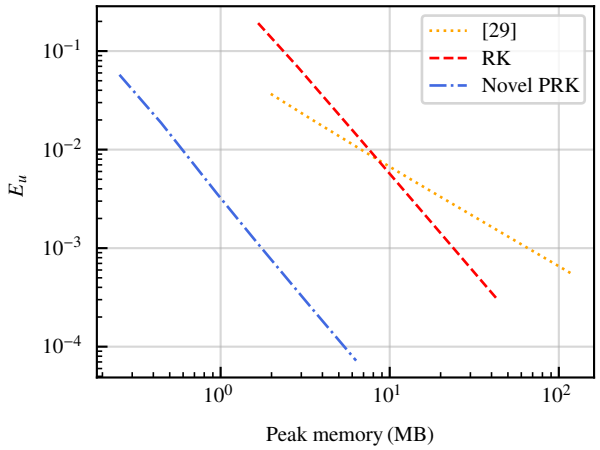

(f) Relative error as a function of peak memory consumption for a particle travelling along the diagonal, i.e., $p_{x,0} = p_{y,0} = 2\sqrt{2}$. The indicated relative error E_u is obtained by adjusting the spatial step size.

Figure 5: Quantitative comparison between the novel PRK method, the RK method and the scheme of [29] for a massless free particle with total momentum centred around four. The remaining parameters of the initial wave function (5) are given by $x_0 = y_0 = 0$ and $\sigma_x = \sigma_y = 1$. The simulation domain ranges from -8 to 8 in both x- and y-direction. The particle is propagated over 0.04. All quantum mechanical quantities are expressed in atomic units. The spatial steps are always chosen equal ($\Delta x = \Delta y$) while the time step is determined by the relevant stability condition as indicated in the text.

Finally, in Fig. 5e and Fig. 5f memory consumption is investigated. Even though all three numerical methods were optimised for speed, avoiding on-the-fly computations as much as possible, some important trends become apparent. The plots illustrate the superiority of the PRK scheme over the RK method in terms of memory consumption. As all values of its four substages need to be stored, memory consumption for the RK method is about five times larger for a certain special step than for the PRK scheme. The required memory for the leapfrog method is even higher. For this second-order accurate scheme, requiring a smaller spatial step, memory consumption can become a prohibitive factor for large-scale simulations.

In another set of results, given in Fig. 6, we study the problem of a massive particle with $m = 0.04$ propagating along the diagonal ($p_{x,0} = p_{y,0} = 2\sqrt{2}$). Other parameters of the initial wave function (5) are the same as for Fig. 5, leading to $mc^2 = 751$ being comparable in magnitude to $p_0 c = \sqrt{p_{x,0}^2 + p_{y,0}^2}c = 548$. Fig. 6a gives the relative error as a function of the time step for a fixed spatial step $\Delta x = \Delta y = 0.10$. The largest simulated time step corresponds to the one determined by the relevant stability condition ((36) for [29], (A.8) for RK and (27) for novel PRK). For time steps near this maximum value, the relative errors of the RK based method and the leapfrog scheme scale as Δt^4 and Δt^2, respectively, indicating that they are dominated by the temporal error. Because we are modelling a massive particle, a factor $\exp\left(-\frac{\imath}{\hbar} mc^2 t\right)$ is introduced into the time-dependent wave function [26]. Accurately describing these fast oscillations is an additional challenge imposed by the (2+1)D Dirac equation, but dealt with accurately by the advocated technique. As we intend to compare the efficiency of the numerical methods in the remaining figures, from now on, we take a three times smaller time step for the RK method than the one given by (A.8). Similarly for the leapfrog scheme, the time step is three times smaller than the one determined by (36). For these choices of the time step, the temporal and spatial error are of the same order yielding a fair comparison between the different methods.

The behaviour of the relative error as a function of the spatial step, which is given in Fig. 6b, is similar to Fig. 5b. All three methods exhibit the expected scaling with respect to the spatial step size. In Fig. 6c, we assess the efficiency of the numerical methods via the total simulation time. It is clear that the novel scheme performs even better for massive particles as its high temporal accuracy is exploited. The cross-over point between the novel PRK based scheme and the leapfrog method is situated some orders of magnitude higher than in Fig. 5c and Fig. 5d. Similar observations are made for the relative error as a function of the peak memory consumption, given in Fig. 6d. In this case too, our

novel method performs considerably better than the other two schemes. Note that the differences would be even more pronounced if we would simulate a particle in the non-relativistic limit, i.e., $mc^2 \gg pc$. Whereas, from Fig. 6, it is evident that our method performs best when a mass is present in the (2+1)D Dirac equation, graphene — perhaps the most important material mentioned in Section 1 — is described by a massless Dirac equation. Still, even in this case the advocated method already outperforms the other schemes (Fig. 5). Moreover, a serious effort is made to introduce a bandgap between the valence and conduction band of graphene to enable fabrication of efficient transistors [58][59]. This bandgap translates to a Dirac equation with mass term, for which this novel scheme is perfectly suited.

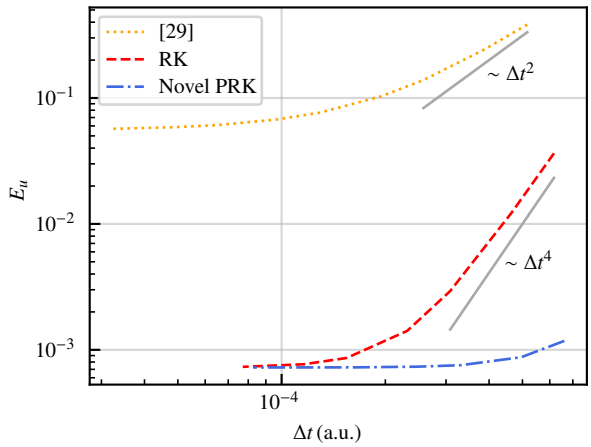

(a) Relative error as a function of the time step for a fixed spatial step $\Delta x = \Delta y = 0.10$. Trendlines are shown in grey.

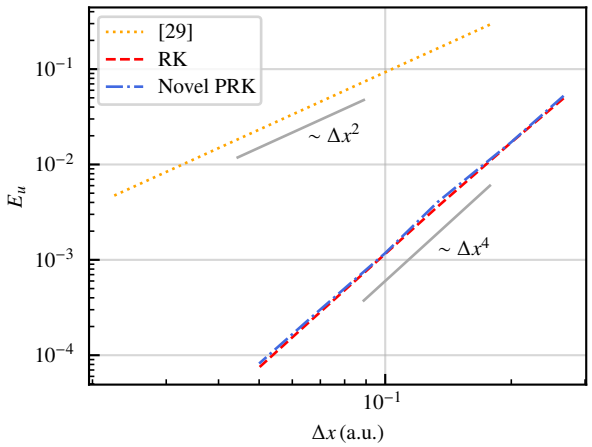

(b) Relative error as a function of the spatial step. Trendlines are shown in grey.

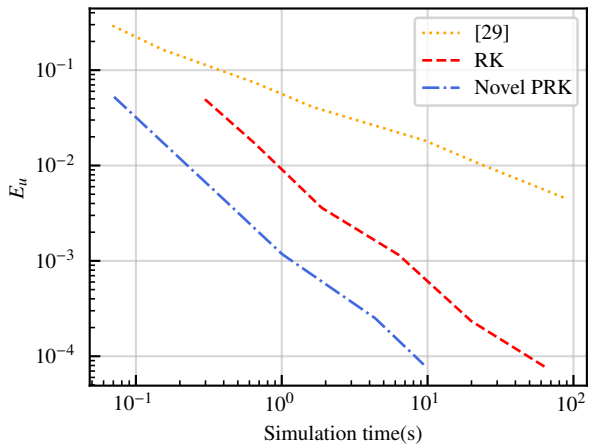

(c) Relative error as a function of the total simulation time. The indicated relative error E_u is obtained by adjusting the spatial step size.

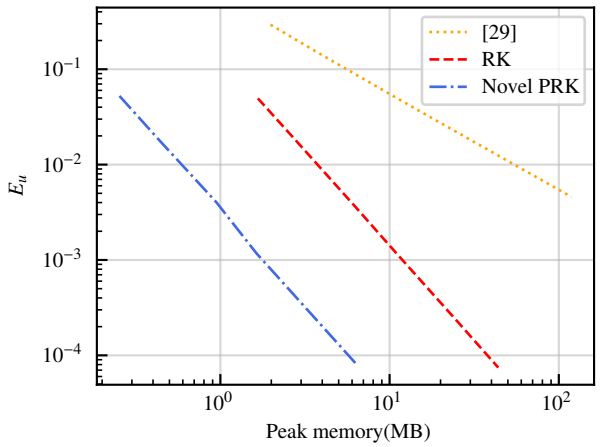

(d) Relative error as a function of peak memory consumption. The indicated relative error E_u is obtained by adjusting the spatial step size.

Figure 6: Quantitative comparison between the novel PRK method, the RK method and the scheme of [29] for a massive free particle travelling along the diagonal. The parameters of the initial wave function (5) are given by $m = 0.04$, $x_0 = y_0 = 0$, $\sigma_x = \sigma_y = 1$ and $p_{x,0} = p_{y,0} = 2\sqrt{2}$. The simulation domain ranges from -8 to 8 in both x- and y-direction. The particle is propagated over 0.04. All quantum mechanical quantities are expressed in atomic units. The spatial steps are equal. For the PRK method the time step in (b)-(d) is determined by (27). For reasons of accuracy, explained in the text, the RK method and the leapfrog method [29] utilise a time step three times smaller than the one determined by (A.8) and (36), respectively.

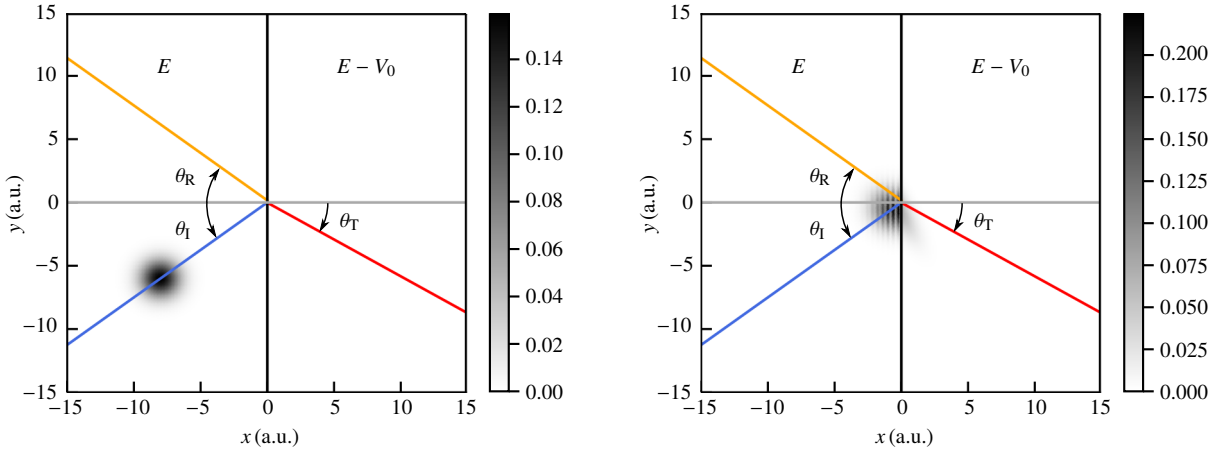

(a) Probability density of initial wave function.

(b) Probability density after 250 time steps.

(c) Probability density after 500 time steps.

Figure 7: Three snapshots of the probability density of a particle incident on a potential step. The parameters of the initial wave function (5) are given by $m = 0$, $x_0 = -8$, $y_0 = -6$, $\sigma_x = \sigma_y = 1$, $p_{x,0} = 8$ and $p_{y,0} = 6$. The simulation domain ranges from -15 to 15 in both the $x-$ and y-direction. A spatial step $\Delta x = \Delta_y = 0.06$ was chosen, which together with $V_0 = 3000$ results in a time step $\Delta t = 2.66\,10^{-4}$. In addition, the relevant angles, θ_I, θ_R and θ_T, of the incident particle, the reflected part of the particle and the transmitted part of the particle, respectively, are indicated.

To further validate the advocated method, we now also include a potential V into the simulations. More specifically, we analyse the behaviour of a particle incident on a potential step. We opt for a discontinuous step at $x = 0$. For $x < 0$ the potential equals 0, while for $x > 0$ it is equal to V_0. For this particular problem, analytical solutions are available only for plane waves. To approximate this situation using a localised gaussian wave packet, we choose the parameters of the initial wave function (5) well, i.e., $p_{x,0}, p_{y,0} \gg 1/\sigma_x, 1/\sigma_y$. In [60], it is illustrated that a Dirac particle incident on a potential step reflects and refracts in the same way as light incident on the interface between two media with a different refractive index. Similarly as for light, incident under an angle θ_I w.r.t. the normal, the angle of refraction θ_T is retrieved by means of Snell's law:

$$E \sin(\theta_\mathrm{I}) = (E - V_0) \sin(\theta_\mathrm{T}), \tag{55}$$

where the refractive indices have been replaced by the kinetic energies E and $E - V_0$, for $x < 0$ and $x > 0$, respectively. Based on (55), we can explain the results of Fig. 7, where three snapshots are shown of a massless particle with $E = 1370$, and incident under an angle $\theta_\mathrm{I} = 36.9°$ onto a potential step with height $V_0 = 3000$. The refracted part

propagates in a direction which is somewhat counterintuitive. Instead of being located in the first quadrant of the xy-plane, the refracted part is in the fourth. The reason for this unexpected behaviour is that $E - V_0$ is negative in this specific case. For a plane wave, via (55), this leads to a negative refraction angle $\theta_T = -30.3°$. By calculating the average momentum in the x- and y-direction of the refracted part, a refraction angle is obtained via our numerical simulation, yielding $\theta_T = -30.2°$. Similarly, we expect $\theta_R = -\theta_I = -36.9°$, while we retrieve $\theta_R = -37.2°$ from the simulation. So, even though we are approximating plane waves by gaussian wave packets, we again obtain excellent agreement between analytical and numerical results for the novel PRK scheme.

9. Conclusion

In this paper, a novel, conservative, fourth-order accurate, real space method for the time-dependent (2+1)D Dirac equation was proposed. A central difference stencil on a staggered grid was utilised to discretise the spatial variables. Employing RK4 to numerically integrate the resulting system of ODEs leads to a method of which the error on the total probability increases over time, severely limiting its applicability. In contrast, our advocated, PRK inspired method exhibits excellent conservation properties. Besides demonstrating this important feature numerically, a rigorous theoretical investigation based on Poisson integrators and backward error analysis was presented too. Furthermore, an easy-to-handle "Courant–Friedrichs–Lewy-like" stability condition was derived and, additionally, the numerical dispersion error proved to be low and isotropic. The novel scheme was validated through some interesting simulation examples. Comparison with the well-established leapfrog method and a higher-order method based on RK4 confirms that our new technique displays superior accuracy and outstanding efficiency, both in terms of total computation time and memory consumption. Giving the growing importance of graphene and comparable materials in nanoelectronic devices for which both quantum mechanical and electromagnetic effects play significant roles, future work will tackle the self-consistent coupling of the Dirac equation with Maxwell's equations as in [61]. Similar as the for the Dirac equation alone, it is expected that conservative higher-order schemes will be effective for the coupled set of equations. Additionally, finite-size effects seriously alter the electronic properties of graphene flakes and nanoribbons and hence, future work will also encompass the inclusion of the proper boundary conditions [62] into the numerical method.

Acknowledgments

The authors would like to thank Research Foundation - Flanders (FWO) for supporting this research (1107321N).

Appendix A.

The RK4 method [34] is readily applied to (2), resulting in the following four substage values, denoted by capitals:

$$\begin{aligned} \mathbf{Y}^{n,1} &= \mathbf{L}\mathbf{y}^n \\ \mathbf{Y}^{n,2} &= \mathbf{L}\left(\mathbf{y}^n + \tfrac{\Delta t}{2}\mathbf{Y}^{n,1}\right) \\ \mathbf{Y}^{n,3} &= \mathbf{L}\left(\mathbf{y}^n + \tfrac{\Delta t}{2}\mathbf{Y}^{n,2}\right) \\ \mathbf{Y}^{n,4} &= \mathbf{L}\left(\mathbf{y}^n + \Delta t\mathbf{Y}^{n,3}\right), \end{aligned} \tag{A.1}$$

while each time step is given by

$$\mathbf{y}^{n+1} = \mathbf{y}^n + \frac{\Delta t}{6}\left(\mathbf{Y}^{n,1} + 2\mathbf{Y}^{n,2} + 2\mathbf{Y}^{n,3} + \mathbf{Y}^{n,4}\right). \tag{A.2}$$

To prove the stability of the RK time stepping scheme, we start from the semidiscretised expression (2). The part of (3) between brackets is Hermitian, which is desired as it relates to the discretised form of the Hamiltonian operator $\hat{\mathbf{H}}$ of (1). Therefore, $\mathbf{L}$ itself is skew-Hermitian and, thus, normal and diagonalisable. Consequently, it suffices to study

$$\frac{\mathrm{d}y}{\mathrm{d}t} = \lambda y \tag{A.3}$$

for all eigenvalues λ of $\mathbf{L}$. Applying RK4 to (A.3) yields

$$y^{n+1} = R(\lambda\Delta t)\, y^n, \tag{A.4}$$

with

$$R(z) = 1 + z + \frac{1}{2}z^2 + \frac{1}{6}z^3 + \frac{1}{24}z^4. \tag{A.5}$$

As $R(\lambda\Delta t)$ is scalar, the condition for Lyapunov stability, described in Section 5, reduces to $|R(\lambda\Delta t)| \leq 1$ for all eigenvalues λ. Similarly as for PRK time stepping (see (25)), we obtain the stability condition:

$$\Delta t \leq \frac{C_{\mathrm{RK}}}{\rho(\mathbf{L})}, \tag{A.6}$$

with $\rho(\mathbf{L})$ being the spectral radius of $\mathbf{L}$. Considering that $\mathbf{L}$ is skew-Hermitian, its eigenvalues λ are purely imaginary, resulting in $C_{\mathrm{RK}} = 2\sqrt{2}$. We remark that the spectral radius of a normal matrix is equal to the 2-norm or spectral norm [63], leading to

$$\rho(\mathbf{L}) = \|\mathbf{L}\|_2 = \sqrt{\lambda_{\max}(\mathbf{L}^\dagger\mathbf{L})} = \sqrt{\rho(\mathbf{L}^\dagger\mathbf{L})}. \tag{A.7}$$

A "Courant-Friedrichs-Lewy-like" condition is obtained after estimation of the spectral radius $\rho\left(\mathbf{L}^\dagger\mathbf{L}\right)$ by the infinity norm $\|\mathbf{L}^\dagger\mathbf{L}\|_\infty$, as in Section 5, yielding

$$\Delta t \leq \frac{C_{\mathrm{RK}}}{\sqrt{\max_i\left(\frac{\left(mc^2 \pm [\mathbf{V}]_{i,i}\right)^2}{\hbar^2} + \left(\frac{7c}{3}\right)^2\left(\frac{1}{\Delta x^2} + \frac{1}{\Delta y^2}\right) + \frac{14c}{3\hbar}|[\mathbf{V}]_{i,i}|\left(\frac{1}{\Delta x} + \frac{1}{\Delta y}\right)\right)}}, \tag{A.8}$$

where $\mathbf{V}$ accounts for $\mathbf{V}_{\mathbf{u}_1}$, $\mathbf{V}_{\mathbf{u}_2}$, $\mathbf{V}_{\mathbf{v}_1}$ and $\mathbf{V}_{\mathbf{v}_2}$. It is not surprising that we get a stability condition akin to (27), given the similarities between $\mathbf{L}$ and $\mathbf{K}$.

To obtain the numerical analogue of the continuous dispersion relation for a free massless particle, i.e., $\omega = \pm kc$ (or $E = \pm pc$), the plane wave expression (28) is substituted into the update scheme (A.1)-(A.2), yielding

$$\omega_{\mathrm{num}} = \frac{\imath}{\Delta t}\ln\left(R(\pm\imath|D|\Delta t)\right), \tag{A.9}$$

with D given by (31), from which it is readily seen that ω_{num} may have a non-zero imaginary part.

References

[1] P. A. M. Dirac, The Quantum Theory of the Electron, Proceedings of the Royal Society A 117 (1928) 610–624. doi:https://doi.org/10.1098/rspa.1928.0023.

[2] C. D. Anderson, The Positive Electron, Phys. Rev. 43 (1933) 491–494. doi:10.1103/PhysRev.43.491.

[3] G. Breit, An Interpretation of Dirac's Theory of the Electron, Proceedings of the National Academy of Sciences 14 (7) (1928) 553–559. doi:10.1073/pnas.14.7.553.

[4] O. Klein, Die Reflexion von Elektronen an einem Potentialsprung nach der relativistischen Dynamik von Dirac, Zeitschrift für Physik 53 (1929) 157–165.

[5] T. O. Wehling, A. M. Black-Schaffer, A. V. Balatsky, Dirac materials, Advances in Physics 63 (1) (2014) 1–76. doi:10.1080/00018732.2014.927109.

[6] A. H. Castro Neto, F. Guinea, N. M. Peres, K. S. Novoselov, A. K. Geim, The electronic properties of graphene, Reviews of Modern Physics 81 (1) (2009) 109–162. doi:10.1103/RevModPhys.81.109.

[7] S. Cahangirov, M. Topsakal, E. Aktürk, H. Šahin, S. Ciraci, Two- and one-dimensional honeycomb structures of silicon and germanium, Physical Review Letters 102 (23) (2009) 1–5. doi:10.1103/PhysRevLett.102.236804.

[8] B. Feng, O. Sugino, R. Y. Liu, J. Zhang, R. Yukawa, M. Kawamura, T. Iimori, H. Kim, Y. Hasegawa, H. Li, L. Chen, K. Wu, H. Kumigashira, F. Komori, T. C. Chiang, S. Meng, I. Matsuda, Dirac Fermions in Borophene, Physical Review Letters 118 (9) (2017) 1–6. doi:10.1103/PhysRevLett.118.096401.

[9] D. Xiao, G. B. Liu, W. Feng, X. Xu, W. Yao, Coupled spin and valley physics in monolayers of MoS 2 and other group-VI dichalcogenides, Physical Review Letters 108 (19) (2012) 1–5. doi:10.1103/PhysRevLett.108.196802.

[10] S. G. Louie, C. H. Park, Making massless Dirac fermions from a patterned two-dimensional electron gas, Nano Letters 9 (5) (2009) 1793–1797. doi:10.1021/nl803706c.

[11] B. Wunsch, F. Guinea, F. Sols, Dirac-point engineering and topological phase transitions in honeycomb optical lattices, New Journal of Physics 10 (2008) 103027. doi:10.1088/1367-2630/10/10/103027.
[12] M. Z. Hasan, C. L. Kane, Colloquium: Topological insulators, Reviews of Modern Physics 82 (4) (2010) 3045–3067. doi:10.1103/RevModPhys.82.3045.
[13] K. Momberger, A. Belkacem, A. H. Sörensen, Numerical treatment of the time-dependent Dirac equation in momentum space for atomic processes in relativistic heavy-ion collisions, Physical Review A - Atomic, Molecular, and Optical Physics 53 (3) (1996) 1605–1622. doi:10.1103/PhysRevA.53.1605.
[14] W. Bao, Y. Cai, X. Jia, Q. Tang, Numerical Methods and Comparison for the Dirac Equation in the Nonrelativistic Limit Regime, Journal of Scientific Computing 71 (3) (2017) 1094–1134. doi:10.1007/s10915-016-0333-3.
[15] W. Bao, J. Yin, A fourth-order compact time-splitting Fourier pseudospectral method for the Dirac equation, Research in the Mathematical Sciences 6 (1) (2019) 1–35. doi:10.1007/s40687-018-0173-x.
[16] X. Antoine, F. Fillion-Gourdeau, E. Lorin, S. MacLean, Pseudospectral computational methods for the time-dependent Dirac equation in static curved spaces, Journal of Computational Physics 411 (2020) 109412. doi:10.1016/j.jcp.2020.109412.
[17] G. R. Mocken, C. H. Keitel, Quantum dynamics of relativistic electrons, Journal of Computational Physics 199 (2) (2004) 558–588. doi:10.1016/j.jcp.2004.02.020.
[18] G. R. Mocken, C. H. Keitel, FFT-split-operator code for solving the Dirac equation in 2+1 dimensions, Computer Physics Communications 178 (2008) 868–882. doi:10.1016/j.cpc.2008.01.042.
[19] J. J. Cao, X. G. Li, J. L. Qiu, J. J. Zhang, Time-compact scheme for the one-dimensional Dirac equation, Discrete Dynamics in Nature and Society 2016 (2) (2016) 1–8. doi:10.1155/2016/3670139.
[20] J. Yin, A fourth-order compact time-splitting method for the Dirac equation with time-dependent potentials, Journal of Computational Physics 430 (2021) 110109. doi:10.1016/j.jcp.2021.110109.
[21] J. W. Braun, Q. Su, R. Grobe, Numerical approach to solve the time-dependent Dirac equation, Physical Review A - Atomic, Molecular, and Optical Physics 59 (1) (1999) 604–612. doi:10.1103/PhysRevA.59.604.
[22] C. Müller, N. Grün, W. Scheid, Finite element formulation of the Dirac equation and the problem of fermion doubling, Physics Letters, Section A: General, Atomic and Solid State Physics 242 (4-5) (1998) 245–250. doi:10.1016/S0375-9601(98)00218-7.
[23] D. Brinkman, C. Heitzinger, P. A. Markowich, A convergent 2D finite-difference scheme for the Dirac-Poisson system and the simulation of graphene, Journal of Computational Physics 257 (PA) (2014) 318–332. doi:10.1016/j.jcp.2013.09.052.
[24] Y. Ma, J. Yin, Error Bounds of the Finite Difference Time Domain Methods for the Dirac Equation in the Semiclassical Regime, Journal of Scientific Computing 81 (3) (2019) 1801–1822. doi:10.1007/s10915-019-01063-5.
[25] Y. Feng, J. Yin, Spatial resolution of different discretizations over long-time for the dirac equation with small potentials, Journal of Computational and Applied Mathematics 412 (10 2022). doi:10.1016/j.cam.2022.114342.
[26] F. Fillion-Gourdeau, E. Lorin, A. D. Bandrauk, Numerical solution of the time-dependent Dirac equation in coordinate space without fermion-doubling, Computer Physics Communications 183 (7) (2012) 1403–1415. doi:10.1016/j.cpc.2012.02.012.
[27] R. Stacey, Eliminating lattice fermion doubling, Physical Review D 26 (2) (1982) 468–472. doi:10.1103/PhysRevD.26.468.
[28] R. Hammer, W. Pötz, Staggered grid leap-frog scheme for the (2 + 1) D Dirac equation, Computer Physics Communications 185 (1) (2014) 40–52. doi:10.1016/j.cpc.2013.08.013.
[29] R. Hammer, W. Pötz, A. Arnold, Single-cone real-space finite difference scheme for the time-dependent Dirac equation, Journal of Computational Physics 265 (2014) 50–70. doi:10.1016/j.jcp.2014.01.028.
[30] R. Hammer, W. Pötz, A. Arnold, A dispersion and norm preserving finite difference scheme with transparent boundary conditions for the Dirac equation in (1+1)D, Journal of Computational Physics 256 (2014) 728–747. doi:10.1016/j.jcp.2013.09.022.
[31] J. Kogut, L. Susskind, Hamiltonian formulation of Wilson's lattice gauge theories, Physical Review D 11 (1975) 395–408.
[32] L. Susskind, Lattice fermions, Physical Review D 16 (1977) 3031–3039.
[33] J. Smit, Introduction to Quantum Fields on a Lattice, Cambridge University Press, 2003.
[34] B. Gustafsson, High Order Difference Methods for Time Dependent PDE, Vol. 38, Springer, 2008.
[35] G. R. Quispel, D. I. McLaren, A new class of energy-preserving numerical integration methods, Journal of Physics A: Mathematical and Theoretical 41 (4) (2008) 045206. doi:10.1088/1751-8113/41/4/045206.
[36] E. Hairer, C. Lubich, G. Wanner, Geometric numerical integration. Structure-preserving algorithms for ordinary differential equations, 2nd Edition, Vol. 31, Springer, 2006.
[37] D. Cohen, E. Hairer, Linear energy-preserving integrators for Poisson systems, BIT Numerical Mathematics 51 (1) (2011) 91–101. doi:10.1007/s10543-011-0310-z.
[38] L. Brugnano, M. Calvo, J. I. Montijano, L. Rández, Energy-preserving methods for Poisson systems, Journal of Computational and Applied Mathematics 236 (16) (2012) 3890–3904. doi:10.1016/j.cam.2012.02.033.
[39] J. M. Sanz-Serna, Symplectic integrators for Hamiltonian problems: An overview, Acta Numerica 1 (May) (1992) 243–286. doi:10.1017/S0962492900002282.
[40] J. M. Sanz-Serna, M. P. Calvo, Numerical Hamiltonian Problems, 1st Edition, Chapman and Hall, 1994.
[41] J. C. Phillips, R. Braun, W. Wang, J. Gumbart, E. Tajkhorshid, E. Villa, C. Chipot, R. D. Skeel, L. Kalé, K. Schulten, Scalable molecular dynamics with NAMD, Journal of Computational Chemistry 26 (16) (2005) 1781–1802. doi:10.1002/jcc.20289.
[42] V. Springel, The cosmological simulation code GADGET-2, Monthly Notices of the Royal Astronomical Society 364 (4) (2005) 1105–1134. doi:10.1111/j.1365-2966.2005.09655.x.
[43] R. Rieben, D. White, G. Rodrigue, High-order symplectic integration methods for finite element solutions to time dependent Maxwell equations, IEEE Transactions on Antennas and Propagation 52 (8) (2004) 2190–2195. doi:10.1109/TAP.2004.832356.
[44] W. Sha, Z. Huang, M. Chen, X. Wu, Survey on symplectic finite-difference time-domain schemes for Maxwell's equations, IEEE Transactions on Antennas and Propagation 56 (2008) 493–500. doi:10.1109/TAP.2007.915444.
[45] J. Shen, W. E. Sha, Z. Huang, M. Chen, X. Wu, High-order symplectic FDTD scheme for solving a time-dependent Schrödinger equation, Computer Physics Communications 184 (3) (2013) 480–492. doi:10.1016/j.cpc.2012.09.032.

[46] Z. Kalogiratou, T. Monovasilis, T. E. Simos, Symplectic integrators for the numerical solution of the Schrödinger equation, Journal of Computational and Applied Mathematics 158 (1) (2003) 83–92. doi:10.1016/S0377-0427(03)00478-3.
[47] C. Xiang, F. Kong, K. Li, M. Liu, A High-Order Symplectic FDTD Scheme for the Maxwell-Schrödinger System, IEEE Journal of Quantum Electronics 54 (1) (2018) 1–8. doi:10.1109/JQE.2017.2782839.
[48] R. Ruth, Canonical integration technique, IEEE Transactions on Nuclear Science 30 (1983) 2669–2671.
[49] B. Leimkuhler, S. Reich, Simulating Hamiltonian Dynamics, Cambridge Monographs on Applied and Computational Mathematics, Cambridge University Press, 2005.
[50] R. Mclachlan, On the Numerical Integration of Ordinary Differential Equations by Symmetric Composition Methods, SIAM J. Sci. Comp. 16 (1995) 151–168. doi:10.1137/0916010.
[51] M. P. Calvo, J. M. Sanz-Serna, The Development of Variable-Step Symplectic Integrators, with Application to the Two-Body Problem, SIAM Journal on Scientific Computing 14 (4) (1993) 936–952. doi:10.1137/0914057.
[52] D. S. Bernstein, Matrix Mathematics: Theory, Facts, and Formulas, 2nd Edition, Princeton University Press, 2011.
[53] P. Decleer, A. Van Londersele, H. Rogier, D. Vande Ginste, Nonuniform and Higher-order FDTD Methods for the Schrödinger Equation, Journal of Computational and Applied Mathematics 381 (2021) 113023. doi:https://doi.org/10.1016/j.cam.2020.113023.
[54] A. Portillo, J. M. Sanz-Serna, Lack of dissipativity is not symplecticness, BIT Numerical Mathematics 35 (2) (1995) 269–276. doi:10.1007/BF01737166.
[55] C. R. Harris, K. J. Millman, S. J. van der Walt, R. Gommers, P. Virtanen, D. Cournapeau, E. Wieser, J. Taylor, S. Berg, N. J. Smith, R. Kern, M. Picus, S. Hoyer, M. H. van Kerkwijk, M. Brett, A. Haldane, J. F. del Río, M. Wiebe, P. Peterson, P. Gérard-Marchant, K. Sheppard, T. Reddy, W. Weckesser, H. Abbasi, C. Gohlke, T. E. Oliphant, Array programming with NumPy, Nature 585 (7825) (2020) 357–362. doi:10.1038/s41586-020-2649-2.
URL https://doi.org/10.1038/s41586-020-2649-2
[56] P. Virtanen, R. Gommers, T. E. Oliphant, M. Haberland, T. Reddy, D. Cournapeau, E. Burovski, P. Peterson, W. Weckesser, J. Bright, S. J. van der Walt, M. Brett, J. Wilson, K. J. Millman, N. Mayorov, A. R. J. Nelson, E. Jones, R. Kern, E. Larson, C. J. Carey, İ. Polat, Y. Feng, E. W. Moore, J. VanderPlas, D. Laxalde, J. Perktold, R. Cimrman, I. Henriksen, E. A. Quintero, C. R. Harris, A. M. Archibald, A. H. Ribeiro, F. Pedregosa, P. van Mulbregt, SciPy 1.0 Contributors, SciPy 1.0: Fundamental Algorithms for Scientific Computing in Python, Nature Methods 17 (2020) 261–272. doi:10.1038/s41592-019-0686-2.
[57] A. Taflove, S. Hagness, Computational Electrodynamics: the Finite-Difference Time-Domain Method, 3rd Edition, Artech House, 2005.
[58] S. Y. Zhou, G. H. Gweon, A. V. Fedorov, P. N. First, W. A. De Heer, D. H. Lee, F. Guinea, A. H. Castro Neto, A. Lanzara, Substrate-induced bandgap opening in epitaxial graphene, Nature Materials 6 (10) (2007) 770–775.
[59] Z. H. Ni, T. Yu, Y. H. Lu, Y. Y. Wang, Y. P. Feng, Z. X. Shen, Uniaxial strain on graphene: Raman spectroscopy study and band-gap opening, ACS Nano 2 (11) (2008) 2301–2305.
[60] P. E. Allain, J. N. Fuchs, Klein tunneling in graphene: Optics with massless electrons, European Physical Journal B 83 (3) (2011) 301–317. doi:10.1140/epjb/e2011-20351-3.
[61] Y. Fu, L. Cao, The Crank–Nicolson Galerkin method and convergence for the time-dependent Maxwell–Dirac system under the Lorentz gauge, Journal of Computational and Applied Mathematics 407 (6 2022). doi:10.1016/j.cam.2021.114007.
[62] L. Brey, H. A. Fertig, Electronic states of graphene nanoribbons studied with the dirac equation, Physical Review B - Condensed Matter and Materials Physics 73 (2006). doi:10.1103/PhysRevB.73.235411.
[63] M. Goldberg, G. Zwas, On matrices having equal spectral radius and spectral norm, Linear Algebra and Its Applications 8 (5) (1974) 427–434. doi:10.1016/0024-3795(74)90076-7.